

## 6. HIGHLIGHTS OF LABORATORY FOR ATMOSPHERES ACTIVITIES IN 1999

### Measurements

#### *Ground-Based Measurements*

##### **Tropospheric Wind Profiling Using Direct Detection Doppler Lidar**

We've achieved two important milestones on the road to using direct-detection Doppler lidar to remotely measure wind profiles from space. The first is the completion of the Mobile Doppler Lidar System. The second is the development and demonstration of a new Doppler lidar receiver for measuring winds.

The mobile Doppler Lidar System is a van-based, multi-purpose lidar. We'll use the lidar in field experiments to measure winds from the surface into the stratosphere. The field measurements will be taken in a variety of atmospheric conditions and can contribute to our understanding of mesoscale atmospheric dynamics and transport. These field experiments will also give us important knowledge about direct-detection Doppler lidar systems. That knowledge will help us develop new satellite versions of these systems. The mobile Doppler lidar system has a modular design that allows us to test such new technologies as lasers, detectors, and telescopes. These technologies will be required for future space-based direct-detection Doppler lidar systems.

The new Doppler lidar receiver is designed to measure winds using the laser signal backscattered directly from air molecules. The first wind profiles measured with this molecular Doppler lidar system were obtained using the Mobile Lidar System operating from GSFC beginning in October 1999 (Figure 2). Profiles of horizontal wind speed and direction as a function of altitude are determined by combining wind velocity information obtained by looking in multiple directions. The lidar points in different directions using the rotating optical scanner mounted on the roof of the van. The altitude is determined by keeping track of the time of flight of the transmitted laser pulse.

In the example shown, wind speed and direction have been determined to an altitude of 35 km with a vertical resolution of 175 m. Winds below 7 km are not shown because the laser signal is too large for the photodetectors to effectively measure. Initial comparisons with co-located rawinsondes show excellent agreement with the lidar measured wind speed and direction. In early 2000, we'll conduct a more extensive measurement program including intercomparison with a variety of other wind measuring systems.

Why is this new capability important? Previous Doppler lidar systems relied on the laser signal backscattered from atmospheric aerosols. The results of these systems are impressive when aerosols are present. However, large areas of the global atmosphere have aerosols insufficient to allow lidar wind measurements from space using these methods. Aerosols are particularly sparse in the mid- to upper troposphere and lower

stratosphere (3-30 km altitude) and over the oceans. In these regions, a Doppler lidar measuring winds using molecular backscatter will be very useful.

Figure 3 is a composite of three different profiles of wind speed that we have obtained from the ground using various implementations of the direct-detection Doppler lidar approach. The profiles are all shown with the same altitude scale. The first two profiles from the left are determined using Doppler receivers optimized for aerosol backscatter operating at a wavelength of 1064 nm. As noted above, the performance of these systems is very good in regions where aerosols are present. This approach is particularly useful for high spatial and temporal resolution studies of atmospheric dynamics in the aerosol-laden boundary layer (0-2 km). The last profile is the most recent result obtained with the molecular backscatter Doppler receiver. The altitude range of the wind measurement is greatly extended, due to the molecular approach and its ability to measure winds from clear air returns.

Many important atmospheric science studies will be aided by spaceborne wind measurements using a Doppler lidar. Improved knowledge of the wind field is an objective of four of the five primary research areas described in the NASA Earth Science Enterprise Science Research Plan. Global wind measurements will also increase under-

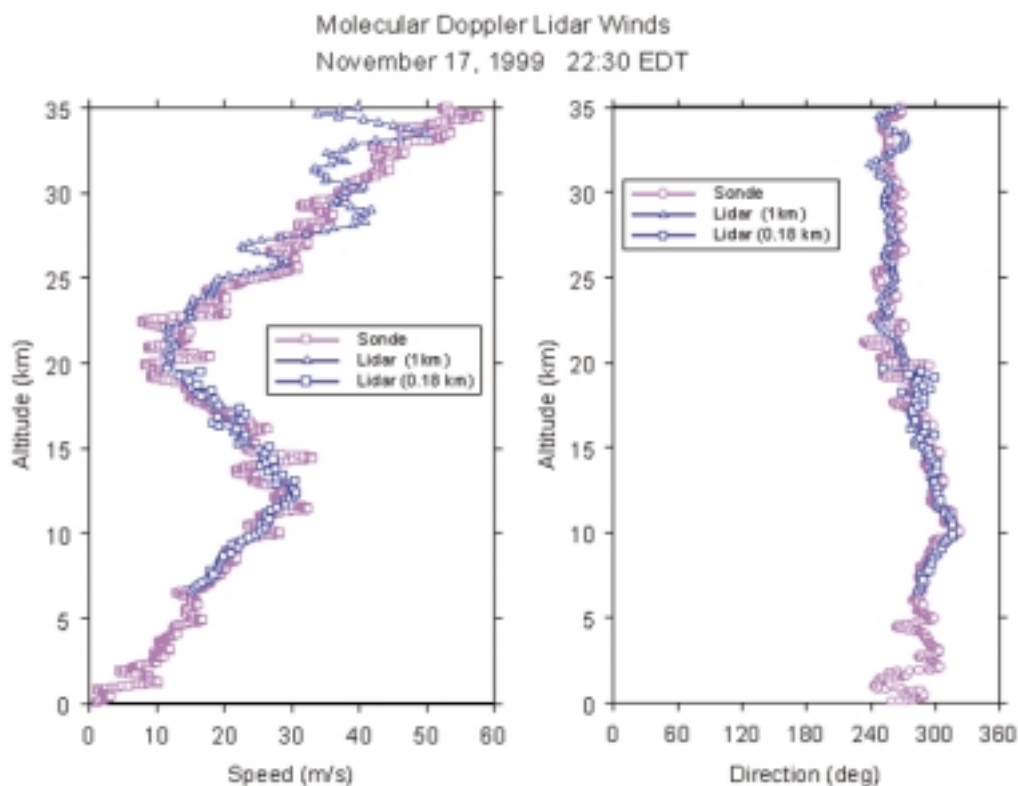


**Figure 2.** Profiles of wind speed and direction obtained with the new molecular Doppler lidar system are shown along with independently determined wind data from a co-located rawinsonde. The molecular Doppler lidar system allows measurement of wind profiles from clear air and thus will be useful in regions of the atmosphere where aerosols are sparse.

standing and prediction of interannual and long-term climate change. Wind data are fundamental to better understanding the role of greenhouse gases, the hydrologic cycle, heat and energy transport, radiative cloud processes, and the biogeochemical cycle. In the area of Natural Hazards Research, global wind measurements would aid in the prediction and tracking of hurricanes and severe storm outbreaks. Finally, wind measurements improve our understanding of the dynamics of weather systems. Including global wind measurements in our models will contribute to significantly improved short- and long-term weather forecasts.

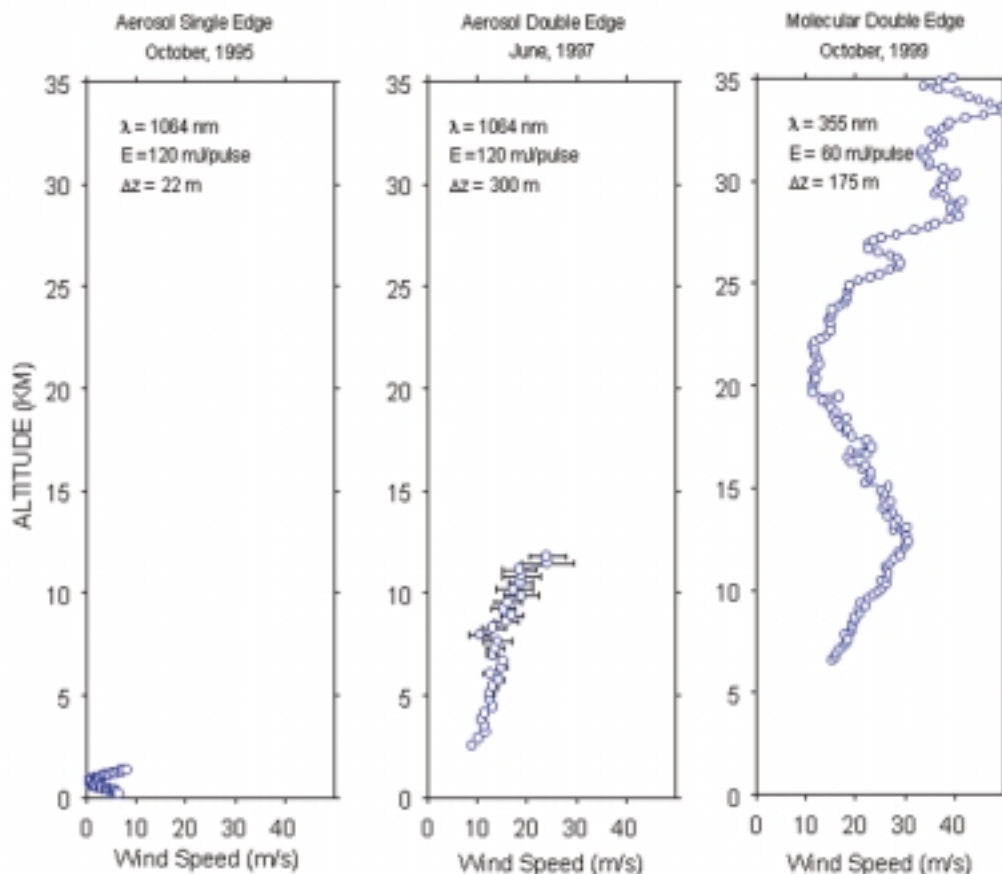


**Figure 3. A composite of three wind speed profiles obtained with different versions of the direct detection Doppler lidar technique. The profiles are shown on the same altitude scale to illustrate the progression of capability, which we have now demonstrated with our ground based lidar program.**

Gentry, B., H. Chen, and S. Li, 2000: Wind measurements with a 355 nm molecular Doppler lidar. Submitted for publication in *Optics Letters*.

Gentry, B., S. Li, S. Mathur, C. L. Korb, and H. Chen, 2000: Doppler lidar measurements of tropospheric wind profiles using the aerosol double edge technique. Submitted for publication in *Applied Optics*.

*Field Campaigns***Distinct Regimes of Amazonian Convection from TRMM Field Campaign Ground-Based Radar Data**

Radar observations of tropical convection in the Amazon region of Brazil during the TRMM-LBA field program are revealing that fundamental changes occur in the organization of precipitation as the large-scale flow pattern evolves during the wet season. These observations may lead to an improvement in the representation of convection in climate models. The observations will also aid in fine-tuning the retrieval of rainfall and latent heating from the TRMM satellite.

Ground-based radars deployed in the Brazilian state of Rondônia for TRMM-LBA provided two months of continuous measurements, every ten minutes, of the precipitation structure of convective systems. We processed the radar reflectivity measurements with techniques that allow us to distinguish active cells of intense convective rainfall from more uniform, widespread stratiform rain. We then applied a preliminary estimate of the conversion of radar reflectivity to rainfall rate. It's too early in the data analysis effort to produce absolute rainfall amounts. Still, we can use the resulting time series to study the time variation of rainfall intensity.

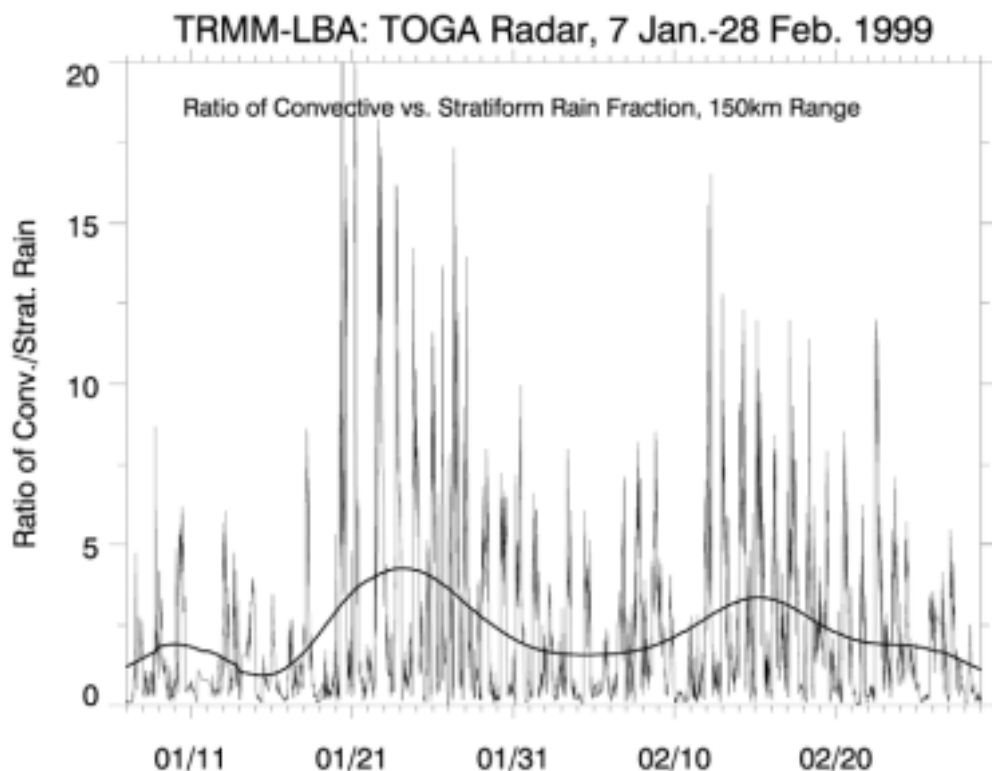
The relative amount of convective versus stratiform rainfall in a convective system highlights important properties, not only of rainfall intensity but also of the vertical distribution in the troposphere of the latent heat of condensation. One way to illustrate how the relative amount of these two kinds of rain structure varies with time is to plot the ratio of convective rain fraction ( $F_c$ ) to stratiform rain fraction ( $1-F_c$ ). This ratio increases exponentially with increasing convective rain fraction and thus emphasizes small changes in convective rain fraction for values of  $F_c$  greater than about 50%.

Figure 4 presents a time series of the ratio of convective rain fraction to stratiform rain fraction from the NASA/NOAA TOGA radar for TRMM-LBA. In two periods, 22-28 January and 10-20 February, precipitation was dominated by convective rainfall. These periods corresponded well to regimes of lower tropospheric easterly wind, as observed from radiosonde data. The intervening occurrence of lower convective vs. stratiform rain fraction was associated with westerly winds at low levels.

Composites of rain statistics between westerly and easterly regimes revealed that rain intensity was 50% higher during easterlies, yet systems were about 50% smaller in area. Furthermore, almost all of the difference in rain intensity between westerly and easterly wind regimes was associated with the convective portion of the rainfall. This implied that an environmental mechanism enhanced the vertical intensity of convective cells and limited the growth of stratiform rain during easterlies and/or limited convective intensity and expanded stratiform rain during westerlies.

This work has important implications for simulating tropical precipitation patterns in global climate models and increasing the accuracy of rainfall retrievals from satellites

such as TRMM. First, we may be able to infer important rainfall and latent heating characteristics of Amazonian convective systems by observing the large-scale wind patterns from conventional data. This could allow us to parameterize these characteristics in GCMs based on relatively simple aspects of flow patterns. Second, we may learn that precipitation and latent heating retrieval algorithms for TRMM perform differently in distinct rainfall regimes. If so, identifying the bulk differences in convective organization based on wind regimes may offer guidance to modify the algorithms and make them more accurate.



**Figure 4.** Time series of the ratio of convective rain fraction ( $F_c$ ) to stratiform rain fraction ( $1-F_c$ ), from the NASA/NOAA TOGA radar during the TRMM-LBA field experiment. The smoothed curve shows the same time series with variability less than eight days removed, which illustrates the variability on weekly time scales.

Rickenbach, T., R. Nieto Ferreira, and J. Halverson, 2000: Relationship between mesoscale properties of convection and large-scale regimes during TRMM-LBA in Rondônia, Brazil. AMS 6th Conference on Southern Hemisphere Meteorology and Oceanography, Santiago, Chile.

#### **Aerosol Recirculation and Rainfall Experiment (ARREX) and Southern Africa Fire-Atmosphere Research Initiative-2000 (SAFARI)**

Aerosol palls cover large expanses of the Earth's surface and arise from biomass burn-

ing, air pollution, dust storms, and other sources. These aerosols may directly scatter solar radiation back to space, thus increasing the Earth's albedo and cooling the Earth's surface and atmosphere. Aerosols also contribute to the Earth's energy balance indirectly. Hygroscopic aerosols act as cloud condensation nuclei and thus affect cloud properties.

Recent TRMM observations over Indonesia provide evidence for the first time that aerosols from biomass burning significantly affect the regional-scale hydrologic cycle. During the satellite's overpass, TRMM radar detected precipitation in smoke-free clouds, but almost none in the smoke-plagued clouds. While the intense smoke from forest fires can completely shut off rainfall, even the more subtle effects of urban pollution may cause significant rainfall reductions. Obviously, to assess the magnitude of such effects in densely populated regions (e.g., Africa, Asia), scientists have to acquire good measurements of aerosol microphysical and chemical properties with which to test the transport and radiation models that would form the basis of such assessments.

Under an agreement between scientists at NASA GSFC and the University of Witwaterand, South Africa, a team has been formed to guide and execute several scientific experiments to study the effects of aerosols on regional climate. The initiative focuses on inserting new technology developed by Goddard for airborne remote sensing (and eventually for spaceflight) and collocated ground-based remote sensing observations for validation. Figure 5 shows two Aerocommander 690 aircraft, provided by South Africa Weather Bureau, equipped with Goddard's remote sensing instruments (right) and University of Witwaterand's microphysical and chemical probes (left).



**Figure 5.** Two aircraft equipped with many remote sensing instruments (right) and microphysical and chemical probes (left) for formation flights. The Goddard's remote sensing instruments contain two shortwave spectrometers and one IR imager, in which the new technology forms the base for Leonardo Airborne Simulator.

In Figure 6, a suite of ground-based radiation instruments is deployed and collocated with aircraft or satellite observations. The scientific objectives are two: (1) to measure broadband shortwave and longwave irradiance at the surface, together with collocated satellite measurements, for studying the radiative energy budget at the Intensive Operations Period (IOP) area, and (2) to acquire narrowband visible, near-IR, microwave radiance measurements and lidar backscattering intensity at the surface for retrieving atmospheric parameters (e.g., column water vapor amount, ozone abundance, aerosol loading and size distribution, etc.).



**Figure 6.** The ground-based remote sensing instruments contain many broadband-short-wave and longwave radiometers (left parts on bench top), narrow-band sunphotometers (right parts on bench top) and spectrometer (center insert at bottom), micro-pulse lidar (left insert at bottom), and scanning microwave radiometer (right insert at bottom).

A huge volume of first-hand data was collected and post-mission calibration and preliminary analysis are underway. The Goddard team has participated in the ARREX wet season campaign (February - March 1999; Bethlehem, South Africa) and the dry season campaign (August - September 1999, Skukuza; South Africa), see Figure 7. An extended field observation is scheduled for August-September 2000, known as SAFARI-2000. The SAFARI-2000 initiative is an umbrella activity, national, regional, and international in nature, aimed at increasing our understanding of the southern African ecological and climate system as a whole, as well as its relationship to hemispheric and global climate.



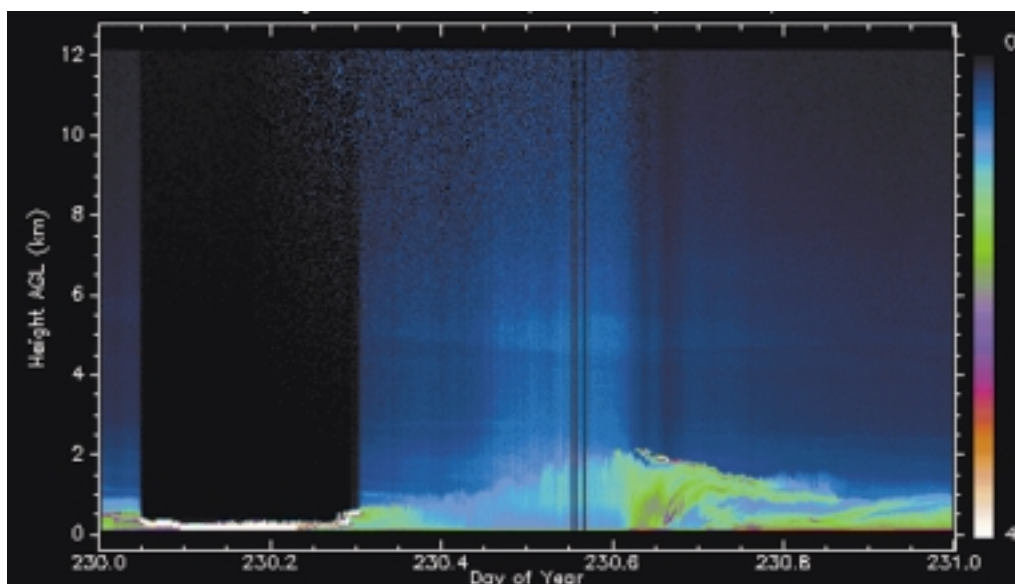


Figure 7. Time series of vertical distributions of biomass burning aerosols observed on 18 August 1999 at Skukuza airport during ARREX dry season campaign. During the night-time (left) the surface site was covered by low level clouds (no lidar return signal above cloud layer); in the morning hours, multiple layers of aerosols were clearly seen (boundary layer capped around 2 km and aloft around 5 km); in the afternoon hours, a heavy smoke layer moved in from the border of Mozambique, about 60 km northeast of Skukuza.

Tsay, S. C., S. Piketh, Q. Ji, J. R. Campbell, and R.J. Swap, 2000. Radiation observations during the Aerosol Re-circulation and Rainfall Experiment (ARREX) in South Africa. *Bull Amer. Meteor. Soc.*, in preparation.

## Data Analysis

### Ozone and Trace Gases

#### Shipboard and Satellite Views of Elevated Tropical Tropospheric Ozone in January-February 1999

Tropospheric ozone is a key oxidant in the atmosphere and, in the upper troposphere, acts as a greenhouse gas. In the tropics, tropospheric ozone interacts with atmospheric dynamical processes both on the large-scale (showing changes during ENSO events, for example) and in convective systems. In addition, chemical influences on ozone are more complex in the tropics than in mid-latitudes because rapidly increasing industrial development, savanna burning, biogenic emissions, and lightning all produce ozone precursors. We use field data to gain insights into these processes and we produce high-resolution satellite maps of tropospheric ozone to give regional views of tropical ozone variability.

Figures 8 and 9 illustrate tropospheric ozone in early 1999 over the tropical Atlantic from in-situ and satellite perspectives, respectively. The altitude-vs-longitude cross-section



tion, from an oceanographic cruise on which daily ozone balloon-sondes were launched between the US and South Africa, shows two tropical sections (Zones 2 and 3, in Figure 8). Figure 9 shows integrated tropospheric ozone from Zones 2 and 3 overlaid on a TOMS map of tropospheric ozone. Agreement between the sonde and satellite data is good, with the satellite showing ozone elevated above background (25 Dobson Units) as an extensive feature from Africa to South America.

In Figure 8, the high ozone at 2-5 km between 8N and the equator originates from biomass burning in northern equatorial Africa. It was a surprise that even higher ozone concentrations were found between 7 and 10 km off southern Africa, which was not burning. Reasons for this “ozone paradox” may be complex. Interhemispheric transport through the Intertropical Convergence Zone (ITCZ) is one possibility, with stable ozone layers entering convective clouds, which transport it from lower troposphere to upper troposphere. The lightning sensor on TRMM shows that many flashes—injecting the essential ozone precursor, nitric oxide (NO), directly into the atmosphere at 7-13 km—are over southern Africa, upwind of the ozone peaks in Zone 3. Water vapor, which destroys ozone photochemically with high efficiency in the tropics, is anticorrelated with ozone in most of the soundings.

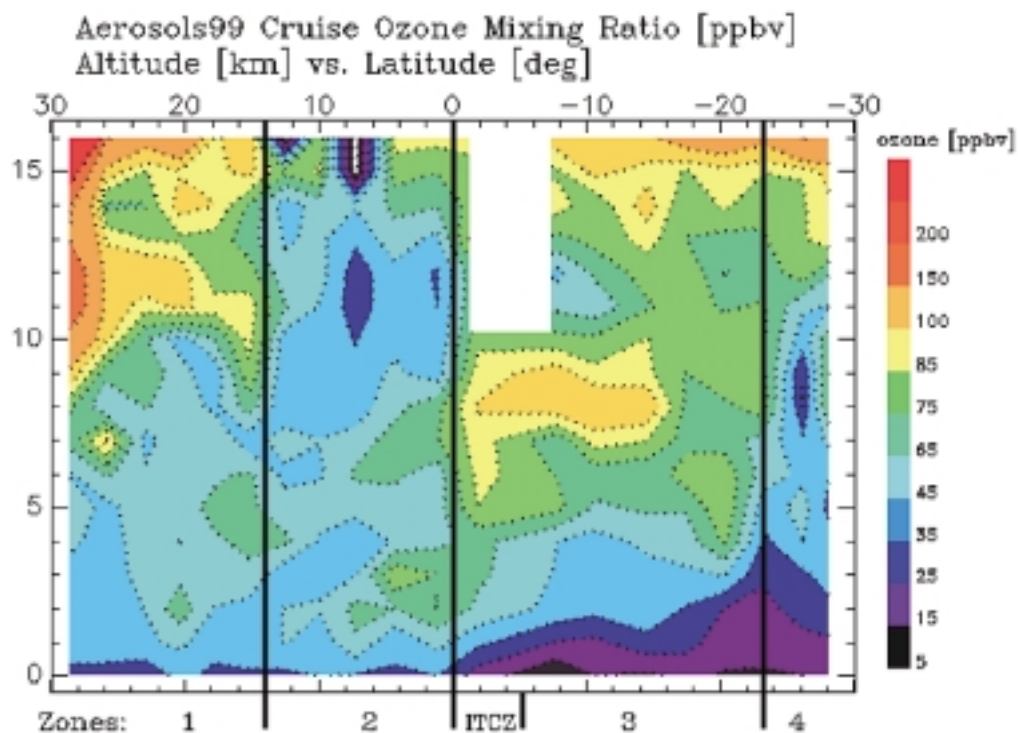


**Figure 8.** TOMS tropospheric ozone (in Dobson Units), averaged over January 1999, with integrated tropospheric ozone from sondes between 21 January and 3 February, shown in white. Gaps in modified-residual tropospheric ozone correspond to persistent clouds, where TOMS data are not used.

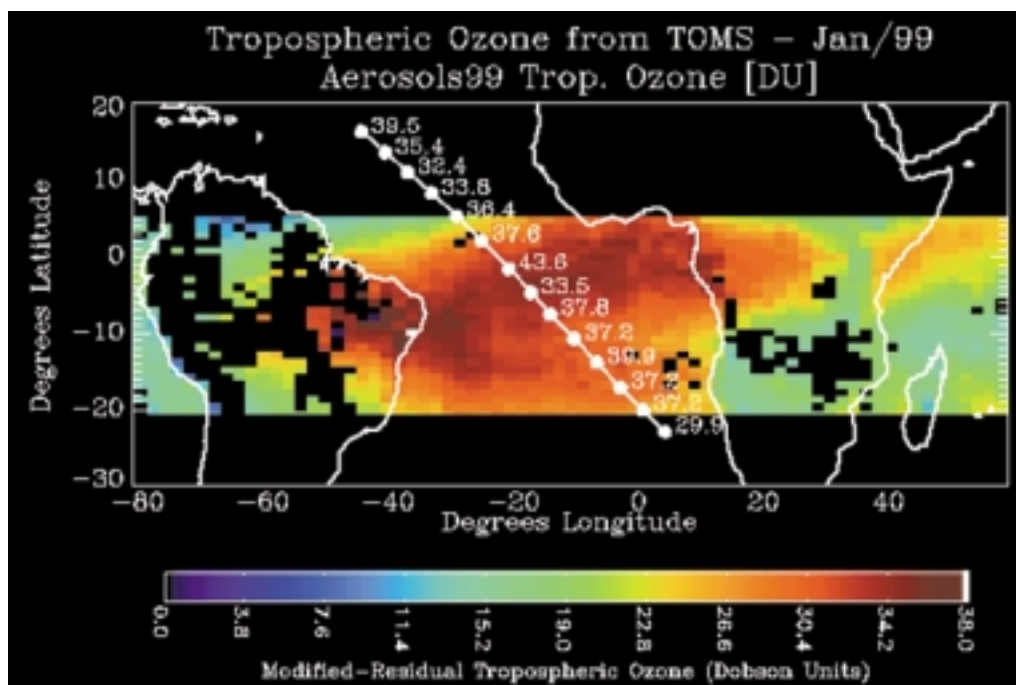


**Figure 9.** From the first North America-to-South African oceanographic cruise with ozonesonde launches (January and February 1999 on board the NOAA Research Vessel Ronald H. Brown), a composite of 22 ozone profiles is shown [altitude in km vs latitude, with ozone mixing ratio in parts per billion volume (ppbv)].

Thompson, A. M., B. G. Doddridge, J. C. Witte, R. D. Hudson, W. T. Luke, J. E. Johnson, B. J. Johnson, S. J. Oltmans and R. Weller, 1999: Shipboard and satellite views of elevated tropospheric ozone over the tropical Atlantic in January-February 1999. *Geophys. Res., Lett.*, submitted.

### Assessment of the Effects of Stratospheric Aircraft

We've participated in assessing the potential atmospheric impacts of a proposed new generation of passenger aircraft. The high-speed civil transport (HSCT) would carry approximately 300 passengers, similar to current airliners. However, the HSCT would travel at more than twice the speed of conventional jetliners. This airplane would cruise at an altitude of 17 to 20 km (56,000 to 66,000 ft).

A primary environmental concern regarding HSCT emissions is the possibility of stratospheric ozone depletion. A flight altitude of 20 km would put the exhaust from the HSCT fleet well into the stratosphere where most of the atmospheric ozone resides (Figure 10). Concern about the impact of aircraft exhaust on ozone contributed to the decision not to develop a supersonic transport in the United States in the 1970s.

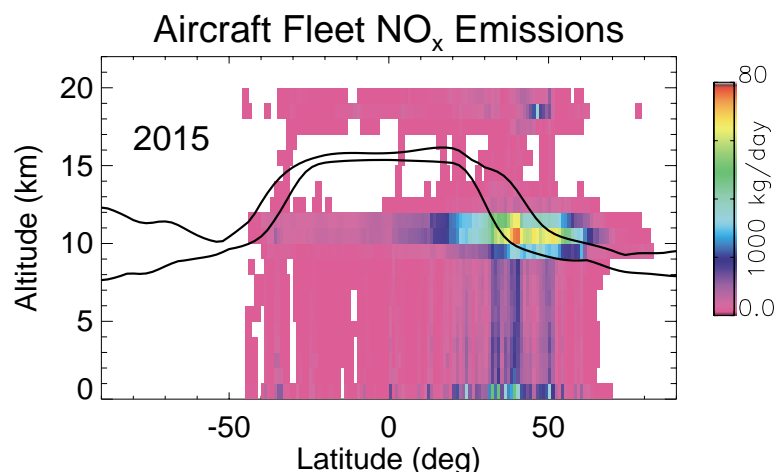


**Figure 10.** Annual average aircraft  $\text{NO}_x$  emissions as a function of altitude and latitude for the year 2015 from the NASA AEAP database. This scenario assumes a fleet of 500 HSCTs operating at an emission index for  $\text{NO}_x$  of 5  $\text{g}(\text{NO}_2)/\text{kg}(\text{fuel})$ , in addition to the projected subsonic fleet background. Emissions above 14 km are from the HSCTs. The range of monthly zonal mean tropopause heights for 1993 is superimposed as solid black lines (from National Centers for Environmental Prediction data).

HSCT exhaust may affect ozone in several ways. The exhaust components of interest for ozone impacts are oxides of nitrogen ( $\text{NO}_x$  (= nitric oxide (NO) + nitrogen dioxide ( $\text{NO}_2$ ))),  $\text{H}_2\text{O}$ , and particulate matter. Engine combustion produces  $\text{NO}_x$ , which is known to participate in one of the main catalytic chemical cycles destroying ozone in the atmosphere. Adding  $\text{NO}_x$  will, in much of the stratosphere, increase the chemical removal rate of ozone. The effect of added  $\text{NO}_x$  in some regions, however, is not so straightforward.  $\text{NO}_x$  interferes with other chemical loss processes and may even contribute to a net increase of ozone in the lowermost stratosphere.

HSCT engines will also produce  $\text{H}_2\text{O}$ .  $\text{H}_2\text{O}$  in the stratosphere is a source of oxides of hydrogen ( $\text{HO}_x$ ), another chemical destroyer of ozone. In addition,  $\text{H}_2\text{O}$  plays a major role in condensation of cloud particles in the stratosphere, which in turn affect the balance of chemicals destroying ozone. Jet engine exhaust is also a source of soot and sulfate particles to the stratosphere. These products will interact with the other exhaust products and the components of the background atmosphere in a non-linear fashion to produce an overall impact on ozone.

The possible interactions of HSCT exhaust with the atmosphere are complex. The net chemical effect of the emissions depends strongly on the transport, dispersion and residence time of the effluent in the stratosphere. The HSCT fleet does not yet exist, and thus its effect cannot be measured. Nor do we have an analogous perturbation to compare it to. Because of this, the potential effects of HSCTs are calculated in numerical models of atmospheric chemistry and transport. Figure 11 shows an example of the changes in total ozone produced by introducing an HSCT fleet into atmospheric models. Such chemical transport models are necessarily incomplete representations of the real atmosphere because we have an incomplete understanding of how the atmosphere

works. Furthermore, computers have limited capacity to simulate the atmospheric system at all time and spatial scales. These factors lead to significant uncertainty in calculation of HSCT impacts. In our current work, we assess the current state of understanding of important processes, our ability to accurately simulate them in models, and the consequent uncertainty in predicted impacts of stratospheric aviation.

### Percent Difference $O_3$ Column Scn 9 - Scn 1

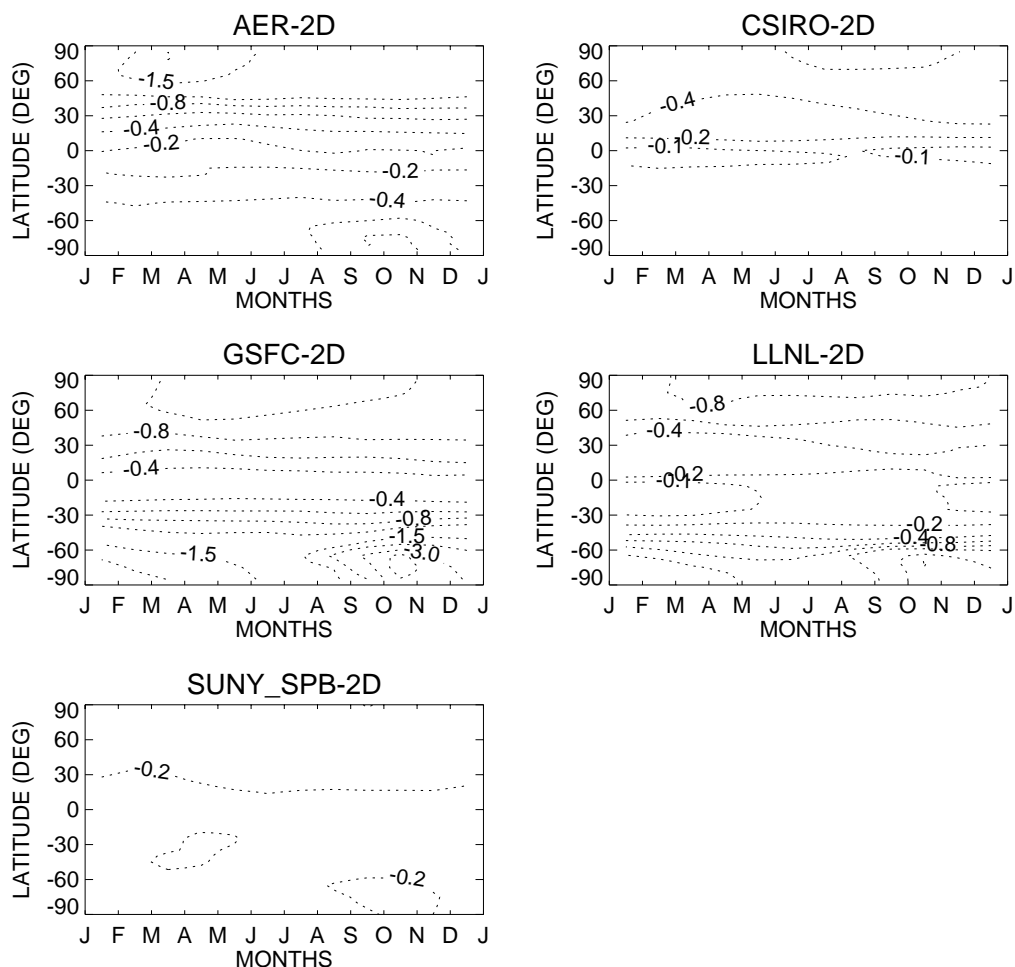


**Figure 11. Seasonal and latitudinal dependence of calculated total column  $O_3$  change in per cent for a scenario including HSCT emissions relative to subsonic aircraft only conditions. The average Northern Hemisphere  $O_3$  change ranges from -0.3 to -0.8% in the 5 models which ran this scenario [Kawa et al., 1999].**

Kawa, S. R., J. G. Anderson, S. L. Baughcum, C. A. Brock, W. H. Brune, R. C. Cohen, D. E. Kinnison, P. A. Newman, J. M. Rodriguez, R. S. Stolarski, D. Waugh, S. C. Wofsy, 1998: Assessment of the effects of high-speed aircraft in the stratosphere. NASA Tech. Pub. 1999-209236, NASA Goddard Space Flight Center, Greenbelt, MD.

*Aerosol Studies***Comparison of TOMS and AVHRR Volcanic Ash Retrievals from the August 1992 Eruption of Mt. Spurr**

The North Pacific air traffic corridors pass over hundreds of volcanoes capable of destroying aircraft through sudden, explosive eruptions. Of equal concern are drifting clouds of volcanic ash that are a serious hazard to aviation even thousand of miles from an eruption. At least 80 aircraft have been damaged since 1980 by flying through volcanic clouds.

Our TOMS instruments have provided much information about the sulfur dioxide content in volcanic clouds. A new analytical technique also allows us to determine ash content and, thus, unambiguously identify volcanic clouds. The UV techniques are very robust and, during daylight hours, can detect both fresh clouds, minutes to hours old, and aging clouds. Data from NOAA's operational AVHRR instruments have also been used to locate volcanic clouds by their visible appearance and, under certain conditions, by spectral differences in ash absorption at thermal infrared wavelengths. The IR measurements are necessary for observations at night but are limited to aging, semi-transparent clouds above a warm surface.

Lately, we've compared UV and infrared retrievals by studying rare, near-simultaneous TOMS and AVHRR observations of the August 19, 1992, Mt. Spurr (Alaska) ash cloud (see Figure 12). Our study demonstrated agreement in key aspects of cloud mass, spatial extent and geometry. Our analysis suggests that we can use the UV TOMS measurements not only to track differences between the ash and sulfur dioxide cloud but also to determine time-dependent ash cloud densities over a broad variety of eruption conditions. This is the focus of a new NASA mission to provide more accurate and timely information on drifting volcanic clouds using a geostationary satellite for high time resolution. The proposed Volcanic Ash Monitor (VOLCAM) camera was recently selected as an alternate NASA ESSP mission and is also being considered as a joint NASA-NOAA experiment on the GOES-O satellite.

Krotkov, N.A., Krueger, A.J., P.K. Bhartia, Ultraviolet optical model of volcanic clouds for remote sensing of ash and sulfur dioxide, *J. Geophys. Res.*, **102**, 21897-21904, 1997.

Krotkov, N. A., O. Torres, C. Seftor, A. J. Krueger, W. Rose, A. Kostinski, G. Bluth, D. Schneider and S. J. Schaefer, Comparison of TOMS and AVHRR volcanic ash retrievals from the August 1992 Eruption of Mt. Spurr, *Geophys. Res. Lett.*, 1999, **26**, 455-458.

Krueger, A.J., Walter, L.S., Bhartia, P.K., Schnetzler, C.C., Krotkov, N.A., Sprod, I. and Bluth, G.J.S., Volcanic sulfur dioxide measurements from the Total Ozone Mapping Spectrometer (TOMS) instruments, *J. Geophys. Res.*, **100**, 14057-14076. 1995.

Seftor, C.J., N.C.Hsu, J.R.Herman, P.K.Bhartia, O.Torres, W.I.Rose, D.J. Shneider, and N.Krotkov, Detection of volcanic ash clouds from Nimbus-7/Total Ozone Mapping Spectrometer, *J. Geophys. Res.*, **102**, 16749-16759, 1997.

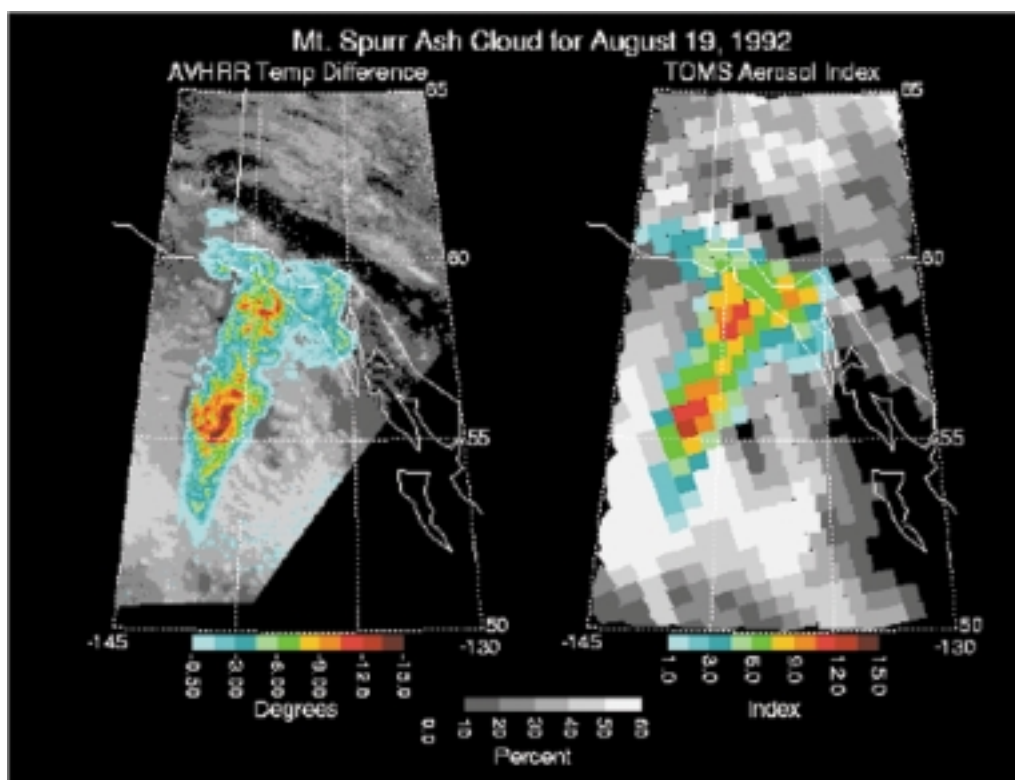


Figure 12. Satellite maps of the August 18, 1992, Crater Peak/Spurr eruption cloud as seen by the NOAA-12 AVHRR instrument and by the NASA's Nimbus-7/TOMS instrument on August 19 at 18:57Z. The AVHRR map (left) shows the brightness temperature difference (T4 -T5 with -0.5K cutoff) as a color scale. The AVHRR band 1 is used to show the reflectivity of underlying water clouds (grey scale). The Nimbus 7 TOMS map (right) shows the Aerosol Index as a color scale. The TOMS 0.38 $\mu$ m band is used to measure the UV reflectivity of water clouds and Earth's surface (the same grey scale).

#### Aerosol and Cloud Distribution in the Indian Ocean Experiment

The Laboratory for Atmospheres participated in the 1999 Indian Ocean Experiment (INDOEX), an international project aimed at determining the proposed regional cooling effect of sulfates and other aerosols over the Indian Ocean. Extremely high aerosol concentrations have been found over the northern Indian Ocean. The majority of these aerosols come from India, but significant amounts are also transported from such areas as Indonesia and Saudi Arabia. The aerosols derive from a complex mixture of urban, biomass, and desert dust sources and have been found to be highly absorbing. In contrast, the southern Indian Ocean is quite clean and represents a typical marine atmosphere.

Members of the cloud and aerosol lidar group used MPL to measure the vertical distribution of aerosols and clouds during INDOEX-99. Measurements were conducted from both the Kaashidhoo Island Observatory (KCO) and from the NOAA ship R/V Ronald H. Brown. KCO is the primary long-term sampling site for the entire INDOEX program, and the MPL was the only lidar system in operation at KCO during the 1999

experiment. The MPL on board the R/V Ronald H. Brown obtained the only continuous lidar data set on a mobile platform, spanning both the southern and northern Indian Ocean. The MPL systems obtained nearly continuous data throughout the experiment and produced the largest lidar data set in all of INDOEX-99.

The initial MPL data analysis is nearly complete. Examples of key data sets include time series of the structure of the aerosol boundary layer (continental outflow layer on top of the marine boundary layer), aerosol optical depth (AOD) of the boundary layer, the lidar ratio, and the identification of elevated cloud layers including thin cirrus (see Figure 13). Selected profiles of aerosol optical properties are also being performed. The results will be presented at the 1999 Fall American Geophysical Union meeting (Welton et al., 1999).

Joint work is also being conducted with other INDOEX-99 participants. The MPL data is being used as part of the satellite comparisons for assessing how well satellite algorithms can determine the AOD. Also, joint work is being conducted with NCAR researchers who have developed a state-of-the-art chemical transport model. Efforts are underway to assimilate the MPL data into the transport model to improve the model's 3-D performance.

The Goddard cloud and aerosol lidar group developed micro-pulse lidars in the early nineties as the first practical technology for full-time unattended lidar measurements. Over twenty instruments are now in use for a variety of international sites and field programs.

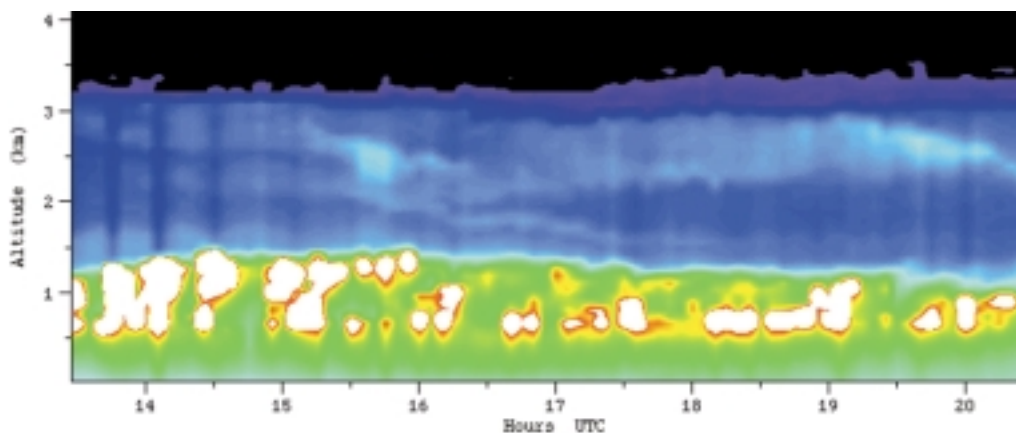


**Figure 13. Aerosol and cloud backscatter cross-sections on March 7, 1999. The marine boundary layer extends to just over 1 km and contains scattered clouds (white). The continental outflow aerosol layer is visible on top and extends to just over 3 km.**

Welton, E. J., P. J. Flatau, K.J. Voss, H. R. Gordon, K. Markowicz, J. R. Campbell, and J. D. Spinhirne, 1999: Measurements of the vertical distribution of aerosols and clouds during INDOEX 1999 using micro-pulse lidars. AGU Fall Meeting Program.



### Angular and Seasonal Variation of Spectral Surface Reflectance Ratios: Implications for the Remote Sensing of Aerosol Over Land

When a satellite views the Earth it “sees” a combination of sunlight reflected from the Earth’s surface (soil, vegetation, oceans) and the Earth’s atmosphere (gases, particles, clouds). In order to use satellite data to learn about the atmosphere, we have to separate the part of the sunlight that reflects off the atmosphere, from the part that reflects off the surface. Luckily we can achieve this separation by using the different wavelengths of the light received at the satellite. The longer wavelengths of the solar spectrum, called the mid-Infrared (mid-IR), penetrate the atmosphere and return information about the surface properties uncontaminated by the atmosphere. In previous work, we demonstrated how the mid-IR could be used to estimate the surface properties of the visible wavelengths that are contaminated by the atmosphere. Using the mid-IR and visible wavelengths together is the key to the difficult problem of separating the signal.

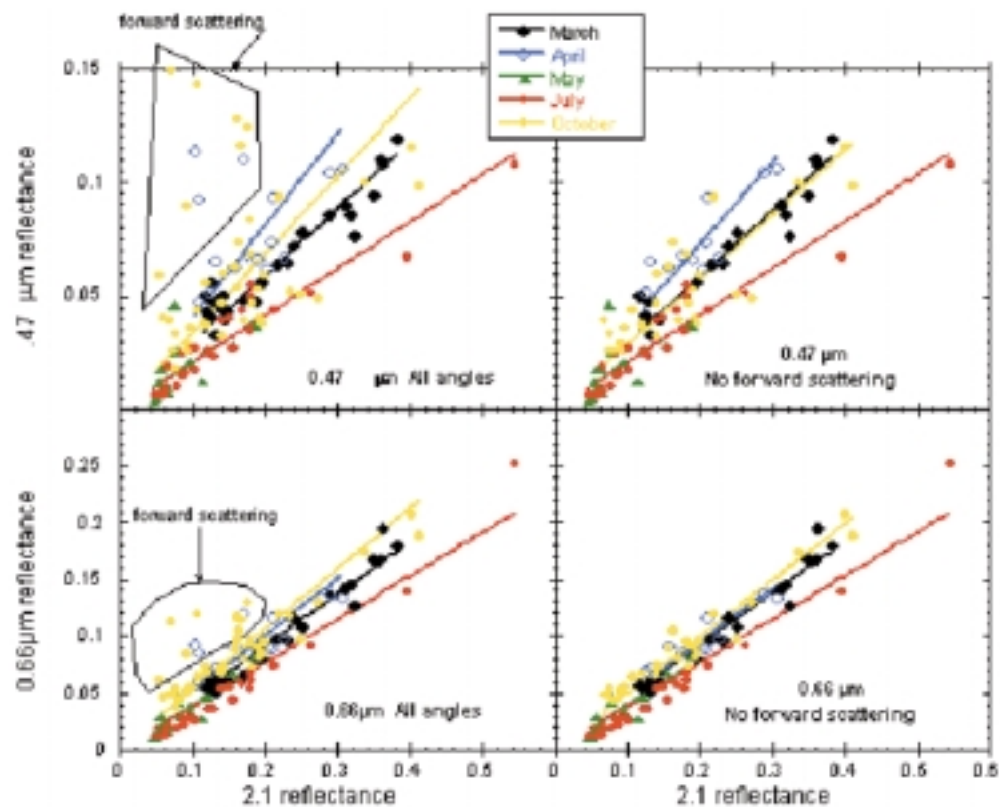


**Figure 14.** Surface reflectance for 0.47  $\mu\text{m}$  (top) and 0.66  $\mu\text{m}$  (bottom) as a function of 2.1  $\mu\text{m}$  surface reflectance with all flights plotted on the same axes. The targets viewed from the forward scattering direction are indicated and removed from the plots on the right hand side, bringing the April and October flights in closer agreement to the other months and to the spectral relationship established from purely nadir data.

In a recent study, we further explored the relationship between the mid-IR and visible reflectance of the surface that allows us to use mid-IR to estimate the visible. Our pre-

vious work revealed relationships between wavelengths that appeared to hold for average conditions almost everywhere. The instruments used to derive these relationships viewed the Earth's surface by looking only in the downward direction. In our recent work, we collected new data from an instrument that permitted variation with angle so that not all of the views were directly downward. We also broadened the time period to include data from early spring to late autumn.

Our results show an unexpected breakdown of the mid-IR/visible relationship when we point the instrument in the sun's direction if the sun is low in the sky (see Figure 14). This breakdown occurs because at special angles the sunlight reaching a vegetated surface is quickly reflected and never has an opportunity to interact with the pigments and liquid water within the leaves. Previous to these results, we were blind to this breakdown at special viewing angles. We would have introduced significant errors into our procedure for separating the satellite signal into surface and atmospheric components. We also found seasonal variations to the relationship between the mid-IR and visible. We are working now to exploit this information on seasonal variability and to improve our procedures.

Remer, L. A., A. E. Wald, and Y. J. Kaufman, 2000: Angular and seasonal variation of spectral surface reflectance ratios: Implications for the remote sensing of aerosol over land., *IEEE Trans. Geoscience Rem. Sens.*, in review.

### ***Clouds and Precipitation***

#### **Approximate Co-Location of Precipitation and Low-Level Zonal Winds in Tropical Monthly Means**

In the tropical monthly mean fields, westerly winds occupy the core precipitation region at low levels (the first 2 km above the surface) in both monsoon and non-monsoon seasons. Figure 15 shows an example of this phenomenon. These westerlies contradict our expectation of trade easterlies in the tropics. (This co-location of precipitation and low-level westerlies is only approximate in that there is a longitudinal phase shift between the two fields. This westerly region is flanked by easterlies to its north and south.)

To analyze this gross tropical circulation feature, we combined theoretical arguments with numerical simulation, using the GEOS GCM and its aqua-planet version. The results show that this gross tropical circulation feature is a natural atmospheric response, crucially influenced by the Earth's rotation, to the monthly-mean convective heating in the tropics. Figure 16 demonstrates the analytic solution. These results also provide a physical basis for cross validation of major NASA satellite missions; i.e., TRMM (tropical heating), QuikSCAT (surface wind), and 4DDA. In the tropical monthly mean fields, westerly winds occupy the core precipitation region at low levels (the first 2 km above the surface) in both monsoon and non-monsoon seasons.

Chao, W. C, and B. Chen, 1999: Approximate co-location of precipitation and low-level westerlies in tropical monthly means. Preprints Volume, American Meteorological Society Eighth Conference on Climate Variations, Sept. 13-17, 195-198.

February: 850 hPa U and Xie–Arkin Precip. (1979 – 1993 average)

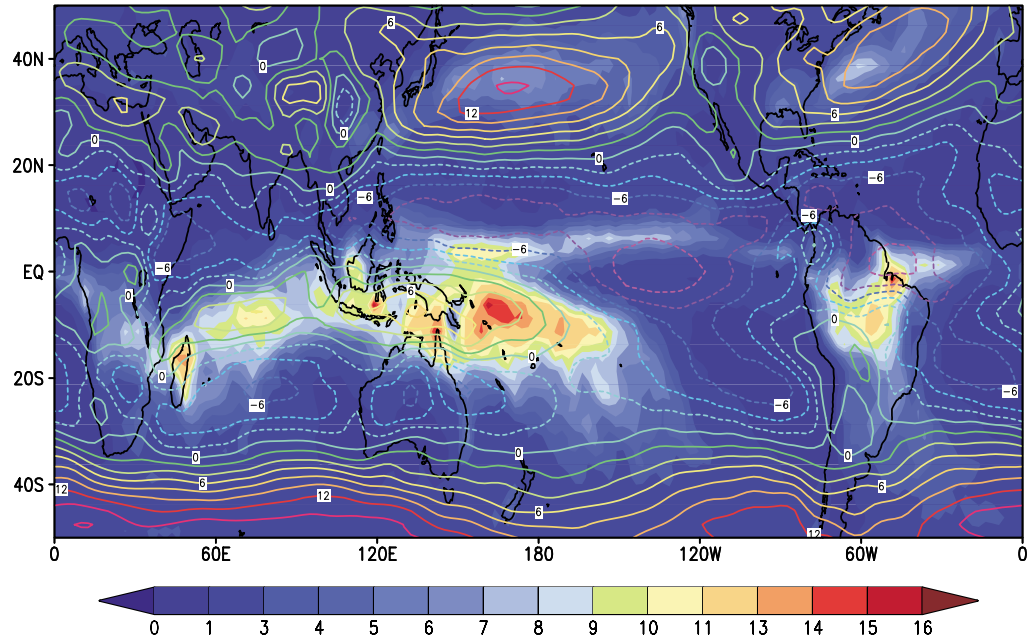


Figure 15. Observed 850 mb zonal wind (in m/s) and precipitation (in mm/day) averaged over four Februarys (1979-1993).

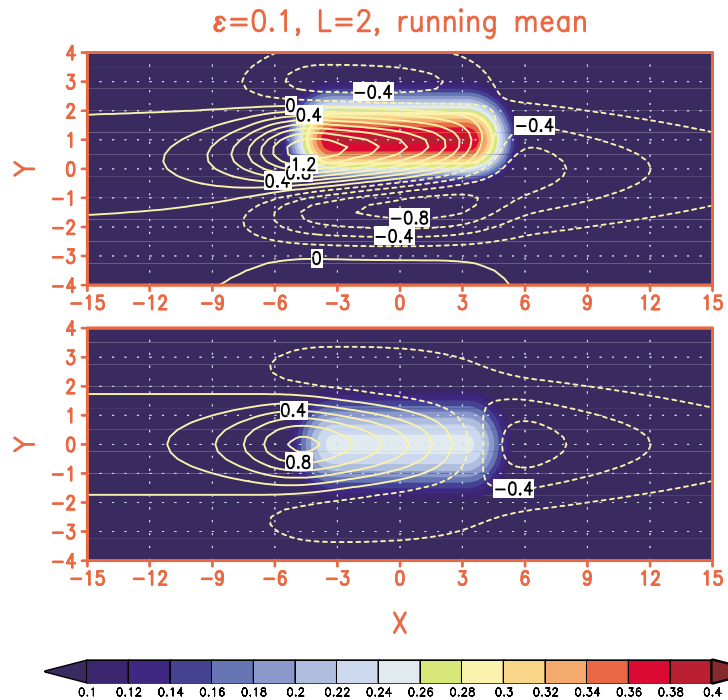


Figure 16. The nondimensional analytic solution of zonal wind response to ITCZ-like convective heating. Unity in length is about 1000 km. The heating region is color shaded and the zonal wind is in contours. The upper (lower) panel is for heating asymmetric (symmetric) with respect to the equator.

### ENSO Precipitation Patterns and Indices

Laboratory staff have developed a global precipitation analysis at monthly time resolution for a 20-year (1979-1999) period as part of the international GPCP. We've used this satellite-based data set to conduct three investigations. Specifically, we've studied the ENSO precipitation patterns during the last 20 years, the evolution of the recent 1997-1999 El Niño/La Niña event, and the similarities and differences between this long-term analysis and the superior rainfall estimates from the TRMM.

We deduced monthly precipitation anomalies (from climatology) and developed ENSO precipitation indices (see Figure 17) based on the rainfall anomalies over the central/eastern Pacific Ocean and over the maritime continent. During an El Niño, it is dry over the East Indies and wet in the central to eastern Pacific. The El Niño Index (EI) at this time has a large positive value, capturing this gradient (see for example 1983, '87, '92, and '97). In major El Niños, including the 1997 event, the EI leads the Pacific SST index because of negative (dry) anomalies over the maritime continent occurring earlier than the central Pacific Ocean warming. During a La Niña the opposite conditions hold true, and these conditions are described by the La Niña Index (LI). The ENSO Precipitation Index (ESPI) is simply the normalized difference of EI minus LI.

The EI and LI are often mirror image. Even so, at the height of an El Niño, (e.g., February 1998) the LI indicates a La Niña essentially at the same time as an El Niño (Figure 17). This apparent paradox is due to the presence of both strong positive and negative rainfall anomalies in the central Pacific leading to a rapid switch from El Niño to La Niña. The precipitation indices are good monitors of the strength and position of the Walker circulation, detecting ENSO events up to two months in advance of traditional temperature indices. These indices are being used to monitor ENSO variations in real time.

We're using the precipitation indices to analyze and compare historic ENSOs and study the associated global precipitation patterns. Figure 18 shows the normalized (by variability) El Niño minus La Niña precipitation anomaly map based on the months of high/low values of the ESPI. The globally complete map shows many of the familiar ENSO features in the tropics. The map also shows newly realized coherent middle- and high-latitude patterns, especially in the Southern Hemisphere.

Initial results of comparing TRMM results to the GPCP fields confirm the ENSO anomalies during 1998 (TRMM was launched in November 1997) and indicate that the TRMM estimates are slightly (10%) higher than the routine GPCP analyses.

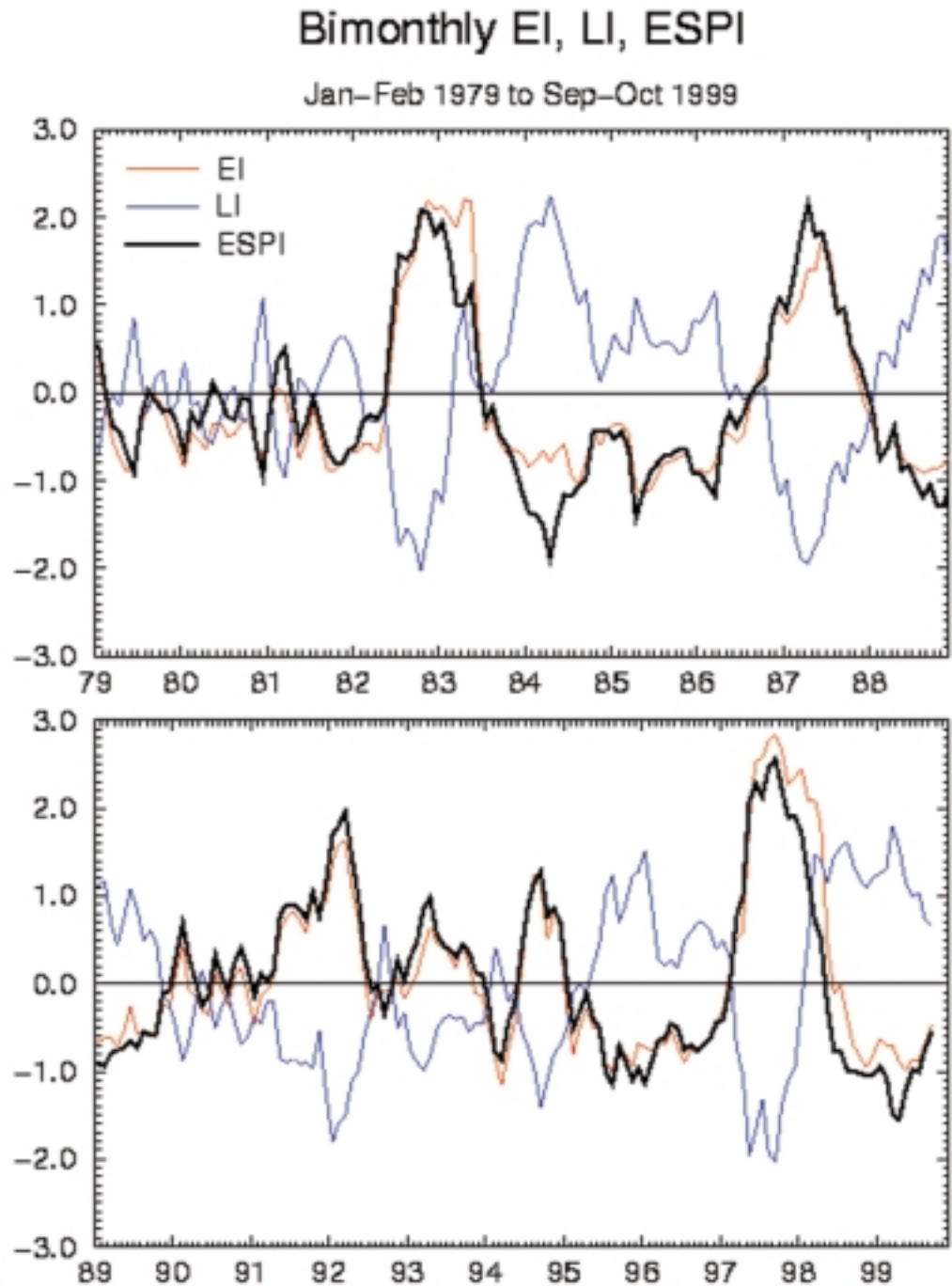
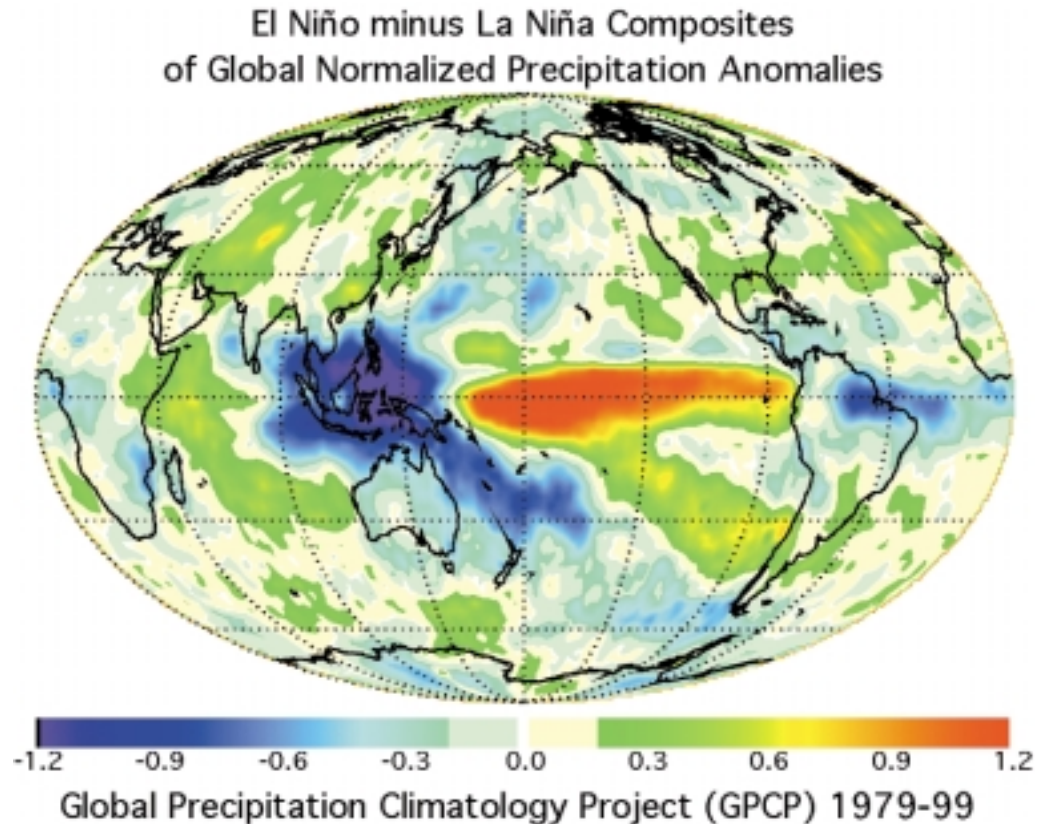


Figure 17. Bimonthly time series of the El Niño Index (EI), the La Niña Index (LI), and the ENSO Precipitation Index (ESPI). Period is January-February 1979 to September-October 1999.



**Figure 18.** Normalized precipitation departures associated with the ENSO Precipitation Index (ESPI) during the period January 1979 to June 1999. Map shows the difference of normalized precipitation anomalies between an 81 month composite of high (El Niño) ESPI values ( $= +0.6$ ) and an 82 month composite of low (La Niña) ESPI values ( $= -0.26$ ).

Adler, R.F., G.J. Huffman, D.T. Bolvin, S.Curtis, E.J. Nelkin, 1999: Tropical Rainfall Distributions Determined Using TRMM Combined with Other Satellite and Raingauge Information, *J. Appl. Meteor.*, submitted.

Curtis, S. and R. Adler, 2000: ENSO indices based on patterns of satellite derived precipitation. *J. Climate*, in press.

Curtis, S., R. Adler, G. Huffman, E. Nelkin, D. Bolvin, 1999: Global precipitation during the 1997-98 El Niño and Initiation of the 1998-99 La Niña. *JGR-Atmospheres*, submitted.



### *Climate Variability and Climate Change*

#### **Cloud, SST, and Climate Sensitivity Inferred from Japan's GMS Measurements**

High-level clouds have a significant impact on the radiation energy budget and, hence, on the climate of the Earth. Laboratory scientists have used data from Japan's GMS to study the relationship between high-level clouds and SST.

Convective cloud systems, which are controlled by large-scale thermal and dynamical conditions, propagate rapidly, within days. At this time scale, changes of SST are small. We used GMS radiances to characterize the relationship between high-level clouds and SST in the tropical western and central Pacific (30S-30N; 130E-170W). In that region, the ocean is warm and deep convection is intensive. We analyzed 20 months of GMS data (January 1998 - August 1999), which comprised the second half of the strong 1997-1998 El Niño. We found that when most of the deep convection moves to regions of high SST, the domain-averaged high-level cloud amount decreases. A +2°C change of SST in cloudy regions results in a relative change of -30% in high-level cloud amount (see Figure 19). This large change in cloud amount is due to clouds moving from cool regions to warm regions, not to the change in SST itself. A reduction of high-level cloud amount in the equatorial region implies a drier upper troposphere in the off-equatorial region. The greenhouse warming of high clouds and water vapor is reduced through increased longwave cooling to space.

Our results are important for understanding the physical processes relating SST, convection, and water vapor in the tropics. They are also important for validating climate simulations using global general circulation models.

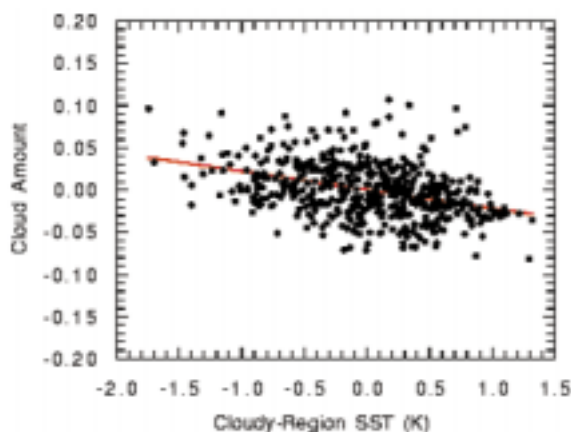


**Figure 19.** Relation between domain averaged high-level cloud amount and the sea surface temperature in cloudy regions in the period January 1998 - August 1999. Each point represents daily mean cloud amount and SST averaged over the domain 30S-30N and 130E-170W. Domain and monthly mean cloud amount and SST are removed, and only the deviations are shown.

Lindzen, R. S., M.-D. Chou, and A. Hou, 2000: Does the earth have an adaptive infrared iris? *Bull. Amer. Meteor. Soc.*, submitted.



### Enhancement of Interdecadal Climate Variability in the Sahel by Vegetation Interaction

For decades, scientists have been trying to understand what caused the paralyzing drought that began in the 1970s, ravaging North Africa and causing the Sahara desert to take over arable Sahel grasslands. Some studies suggested that by using the land for farming and livestock grazing, humans were responsible for bringing about the drought and keeping the land from recovering. New research conducted by a team of Goddard and UCLA scientists shows that although a human hand can't be absolutely ruled out as a factor, the devastating drought may be a completely natural phenomenon, fueled by the land's naturally-changing vegetation cover.

In a paper to appear in *Science*, the Goddard/UCLA team described how vegetation dynamics might play a key role in leading to the interdecadal variation of drought in the Sahel during the 1970s, 80s and early 90s. The team used a biomass model coupled with an atmospheric general circulation model to simulate the growth and decay of vegetation in response to rainfall, sunlight, evapotranspiration and photosynthetic processes. The investigators found that interactive vegetation provides a positive feedback, more than doubling the severity of the long-term Sahelian drought, which was initiated by anomalous sea surface temperatures. This is the first time the effect of vegetation dynamics on long-term climate variability has been demonstrated in a realistic global model (see Figure 20).

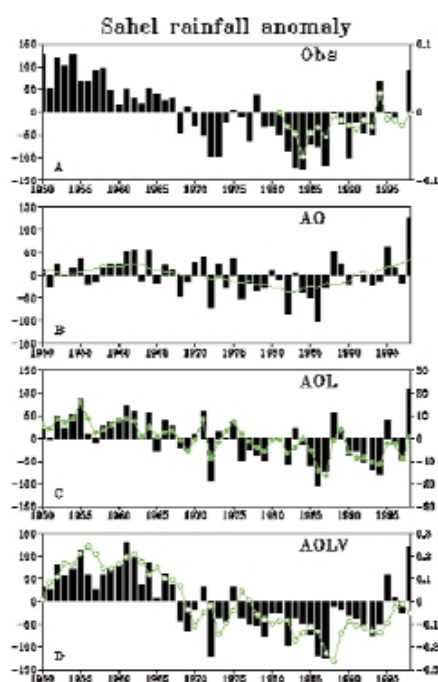


**Figure 20.** Annual rainfall anomaly in mm-y<sup>-1</sup> (vertical bars) over the West African Sahel (13N-20N, 15W-20E) from 1950 to 1998: (A) observations from Hulme (1); (B) model with non-interactive land-surface hydrology (fixed soil moisture) and non-interactive vegetation (SST influence only, AO); smoothed line is a 9-year running mean showing the low-

frequency variation; (C) model with interactive soil moisture and vegetation (AOLV). Also plotted (as connected circles; labeled on the right ) are: (A) the Normalized difference Vegetation Index (NDVI) (31); (C) model simulated annual soil moisture anomaly (mm); (D) model simulated leaf area index (LAI) anomaly. All the anomalies are computed relative to the 1950-98 base period except that the NDVI data is relative to 1981.

Zeng, N., D. Neelin, W. Lau, and C. Tucker, 1999: Enhancement of Interdecadal Climate Variability in the Sahel by Vegetation Interaction. *Science*, **286**, 1537-1540.

## Modeling

### Data Assimilation

#### Improving Four-Dimensional Global Data Sets and Short-Range Forecasts Using TRMM and SSM/I-Derived Rainfall and Moisture Observations

Laboratory for Atmospheres research has shown that satellite data on rainfall and moisture can significantly enhance global data sets and short-term forecasts in the tropics. Assimilating satellite data improves not only the hydrological cycle but also key climate parameters in analyses produced by the GEOS DAS. Specifically, we investigated the impact on GEOS products of assimilating TRMM Microwave Imager (TMI) and SSM/I-derived rainfall and total precipitable water (TPW) observations.

Figure 21 shows the results of assimilating 6-hour averaged rainfall and TPW in the GEOS analysis for January 1998. We assimilated rainfall and TPW data that others produced. The figure presents the effect of that data on four of the parameters we examined: tropical precipitation, TPW, outgoing longwave radiation (OLR), and outgoing shortwave radiation (OSR). The monthly-mean spatial biases and error standard deviations are substantially reduced.

The apparent exceptions are biases in the tropical-mean precipitation and OLR. The slightly larger precipitation bias suggests that the rainfall assimilation algorithm is more effective in reducing precipitation than in enhancing it. The apparent increase in the OLR bias reflects the virtual elimination of the negative OLR bias associated with errors in precipitation. This change produces a tropical-mean bias dominated by the positive (but reduced) bias in the rain-free regions.

Overall, rainfall assimilation reduces the state-dependent errors in the moisture field to improve the longwave radiation in clear-sky regions. The OSR errors in the GEOS analysis are dominated by errors in clouds. The improved OSR indicates improved cloud patterns.

Our improved analysis also leads to better short-range forecasts in the tropics, as shown in Figure 22. This work demonstrates the potential of using space-based rainfall and TPW observations for improving numerical weather prediction and the quality of assimilated global data sets for climate research.

Hou, A. Y., D. Ledvina, A. da Silva, S. Zhang, J. Joiner, R. Atlas, G. Huffman, and C. Kummerow, 2000: Assimilation of SSM/I-derived surface rainfall and total precipitable water for improving the GEOS analysis for climate studies, *Mon. Wea. Rev.*, **128**, 509-537.

Hou, A. Y., S. Zhang, A. da Silva, W. Olson, 2000: Improving assimilated global datasets using TMI rainfall and columnar moisture observations, *J. Climate*, in press.

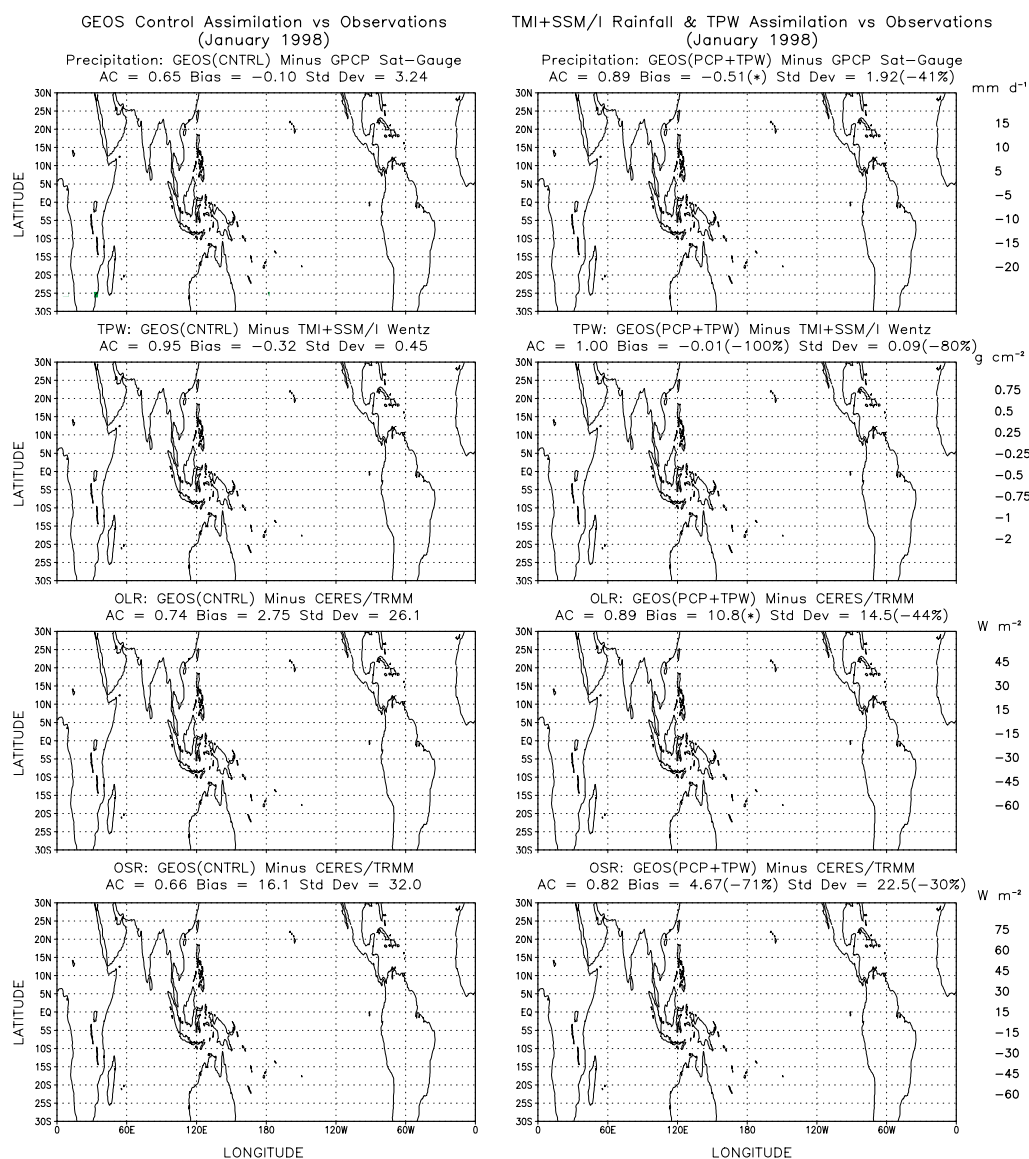


**Figure 21.** NASA GEOS assimilation results with and without TMI and SSM/I observations for January 1998. Left panels show errors in the monthly-mean tropical precipitation, total precipitable water, outgoing longwave radiation, and outgoing shortwave radiation in the GEOS control assimilation. Right panel shows the impact of assimilating TMI and SSM/I rainfall and TPW observations on these fields. Percentage changes relative to errors in the GEOS control are given in parentheses.

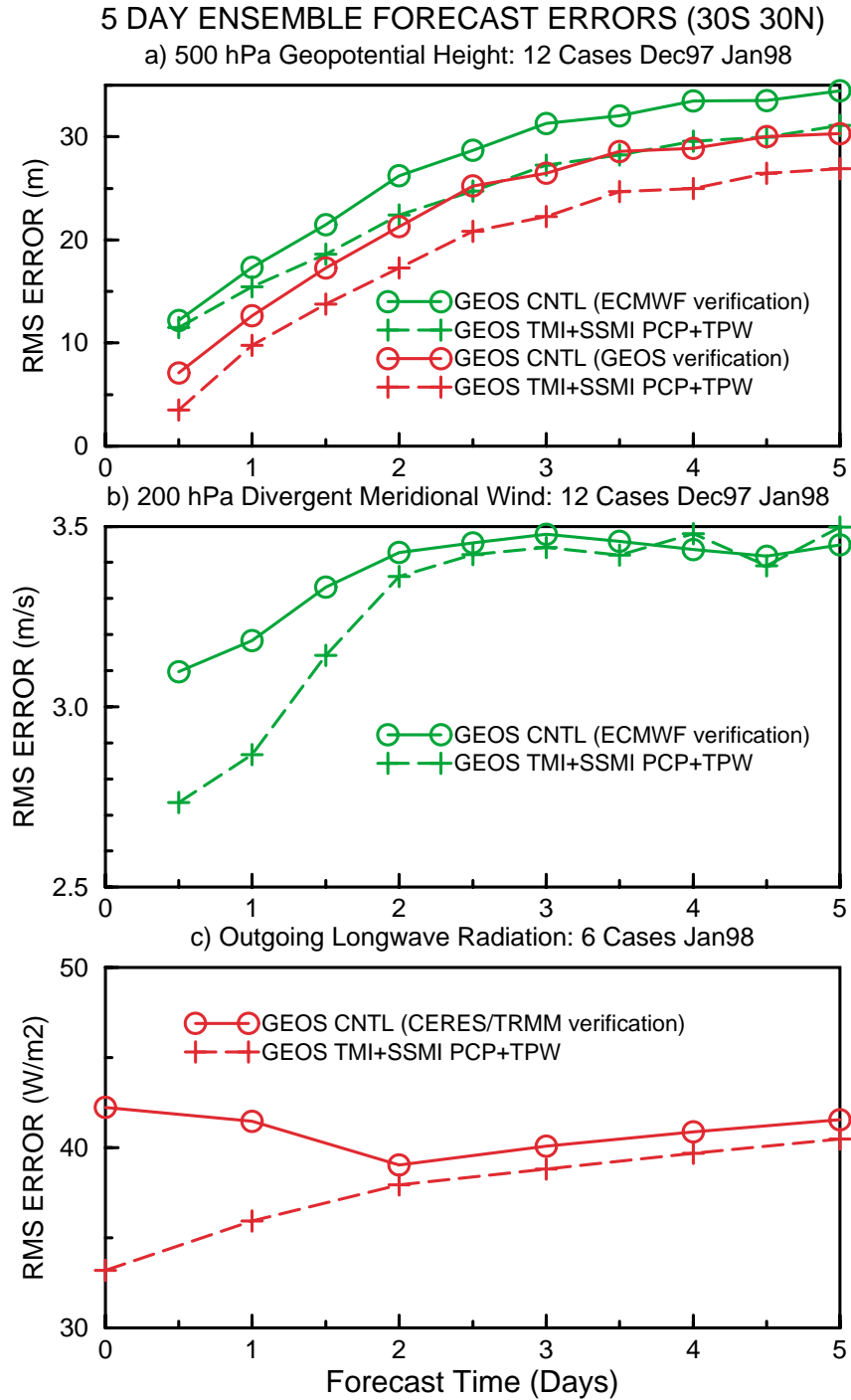


**Figure 22.** (a) Five-day ensemble forecast rms errors in tropical geopotential height at 500 hPa. Results in green are verified against the ECMWF analysis and results in red are verified against the average of the GEOS control analysis and the TMI and SSM/I rainfall and TPW assimilation. (b) Same as (a) except for the 200 hPa divergent meridional wind verified against the ECMWF analysis. (c) Same as (a) except for the OLR verified against CERES/TRMM observations.

### 1-D Variational Retrieval of Temperature and Humidity from GPS/MET

The Laboratory for Atmospheres has collaborated with Meteo France and the Jet Propulsion Laboratory in developing a technique for retrieving temperature and humidity simultaneously from Global Positioning Satellite (GPS) data. The technique is a 1-dimension variational (1DVAR) analysis of radio occultation refractivity data from the GPS.

We validated temperatures retrieved from GPS with nearby radiosonde data. Our analysis shows that GPS can accurately measure tropopause temperatures. The GPS data has a vertical resolution similar to radiosonde data. In addition, the GPS has the advantage of observing areas not covered by the existing radiosonde network. The results also show that accurate temperatures can be obtained from GPS data in a cost-effective manner (i.e. analysis can be done on existing workstations or PC's).

The 1DVAR was shown to be superior to the more traditional approach of assuming a humidity profile to retrieve a temperature profile. This so-called direct retrieval lacks the 1DVAR's highly accurate first guess temperature derived from a numerical weather prediction model forecast (see Figure 23).

Occultation: Lat 58.94deg, Lon -85.86deg, 1995 07 03, 12:21UTC, Transmitter 18

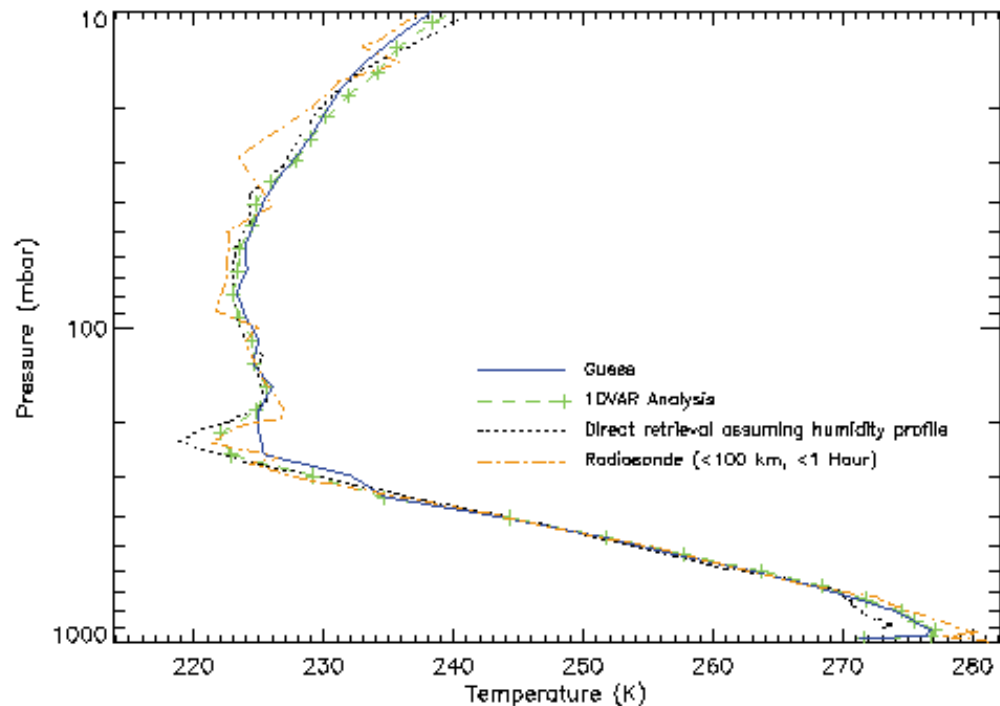


**Figure 23.** Example of a single GPS temperature retrieval by two methods: 1DVAR and direct retrieval. The model's first guess for the 1DVAR is shown (solid line) as well as a collocated radiosonde. Note that both retrievals capture the cold tropopause seen by the radiosonde. However, the 1DVAR gives an improved result in the lower troposphere.

Poli P., J. Joiner, E. R. Kursinski, and M. Kolodner, 2000: 1DVAR analysis of temperature and humidity using GPS radio occultation data. Preprint of the 10th Conference on Satellite Meteorology and Oceanography, 80th AMS, Long Beach, CA, January 9-14.

Poli P., J. Joiner, and E. R. Kursinski, 2000: 1DVAR analysis of temperature and humidity using GPS radio occultation data. *J. Geophys. Res.*, to be submitted.

### ENSO and Weather

We've learned that our ability to predict short-term climate variations depends on whether the ENSO is in a warm or cold phase.

The ENSO, is characterized by major changes in the tropical Pacific SSTs. Widespread warming of the central and eastern tropical Pacific occurs during EL Niño, and widespread cooling occurs during La Niña.

The ENSO phenomenon also has major impacts on the weather over many parts of the globe. The impact of ENSO on middle latitudes is particularly strong in the Pacific/North American region during the winter. To understand the link between weather and the anomalous tropical Pacific SSTs associated with ENSO, we must know how the SSTs impact the larger scale (planetary) waves. Furthermore, we need to understand how the planetary scales affect, and are affected by, weather.

ENSO's effect on the middle latitudes extends beyond the atmosphere's seasonal average response to SSTs. ENSO also modulates the variability and intensity of the planetary waves and weather systems. This influence is manifest, for example, as a change in the sensitivity to initial conditions in forecasts run with a GCM.

In Figure 24, we show the results of 27 seasonal forecasts for the 1983 El Niño and the 1989 La Niña events, using an early version of the GEOS GCM. The forecasts are for January through March (JFM) and are started 15 days earlier in mid-December using SST and sea ice specified from observations. The 27 forecasts for each year differ only in that they are started from slightly different initial conditions.

Figures 24a and 24b show selected stream lines at 200mb for the 27 JFM forecasts. There is a clear difference in the "spread" or noise in the seasonal forecasts for the two years. The 1998 La Niña event displays considerably greater noise or sensitivity to initial conditions in the Pacific region. The greater noise reflects a more frequent occurrence of blocking highs and quasi-stationary low pressure anomalies during 1989 compared with 1983. Figures 24c and 24d show the mean zonal wind and E-vectors associated with the JFM anomalies at 200mb.

How can we explain this difference? During 1983 the jet is extended eastward across the United States, while during the cold event (1989) the jet is retracted. During both years the E-vectors point up the gradient of the jet indicating that the noise is gaining

energy from the jet. During 1989 the E-vectors are, however, much larger. Their size indicates a much greater generation of noise (or uncertainty) for the retracted jet.

Figure 25 shows the variability of the 500mb height field associated with weather systems (time scales less than 10 days). Figures 25a and 25b show the case-to-case variability of the weather variance. The contours represent a particular value of the weather variance plotted for all 27 members. Comparing 1983 to 1989, we see that during the La Niña year the weather systems tended to be diverted to the north over the eastern Pacific.

Consistent with Figure 24b, 1989 also shows more north/south scatter in the position of the Pacific storm track. This pattern suggests considerable uncertainty in the statistics of the storm systems moving onto the west coast of North America. The mean difference in the weather variance between the two years (Figure 25c) highlights the tendency for weather systems to occur further north during the cold event.

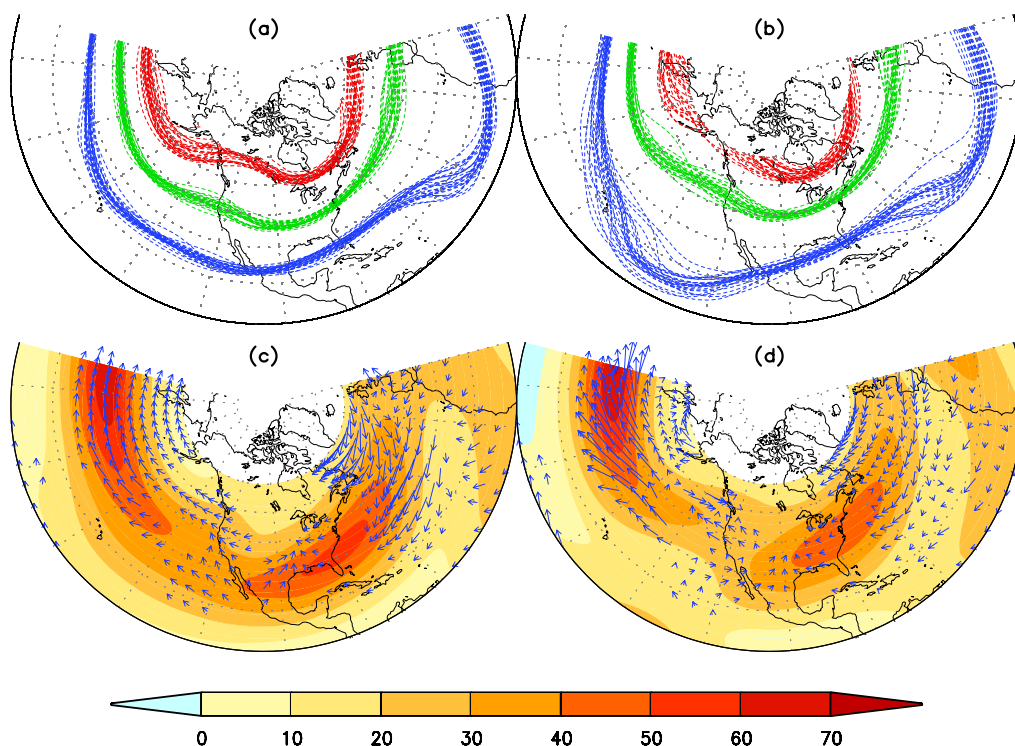


**Figure 24:** (a) Three different stream lines of the 1983 JFM stream function at 200 mb plotted for all 27 ensemble members. (b) The same as (a) but for 1989. (c) The 200 mb zonal wind (shaded), and the extended E-vectors computed from the intra-ensemble variability of the 1983 JFM mean winds at 200 mb. (d) Same as (c) but for 1989. Units for the u-winds are m/s.



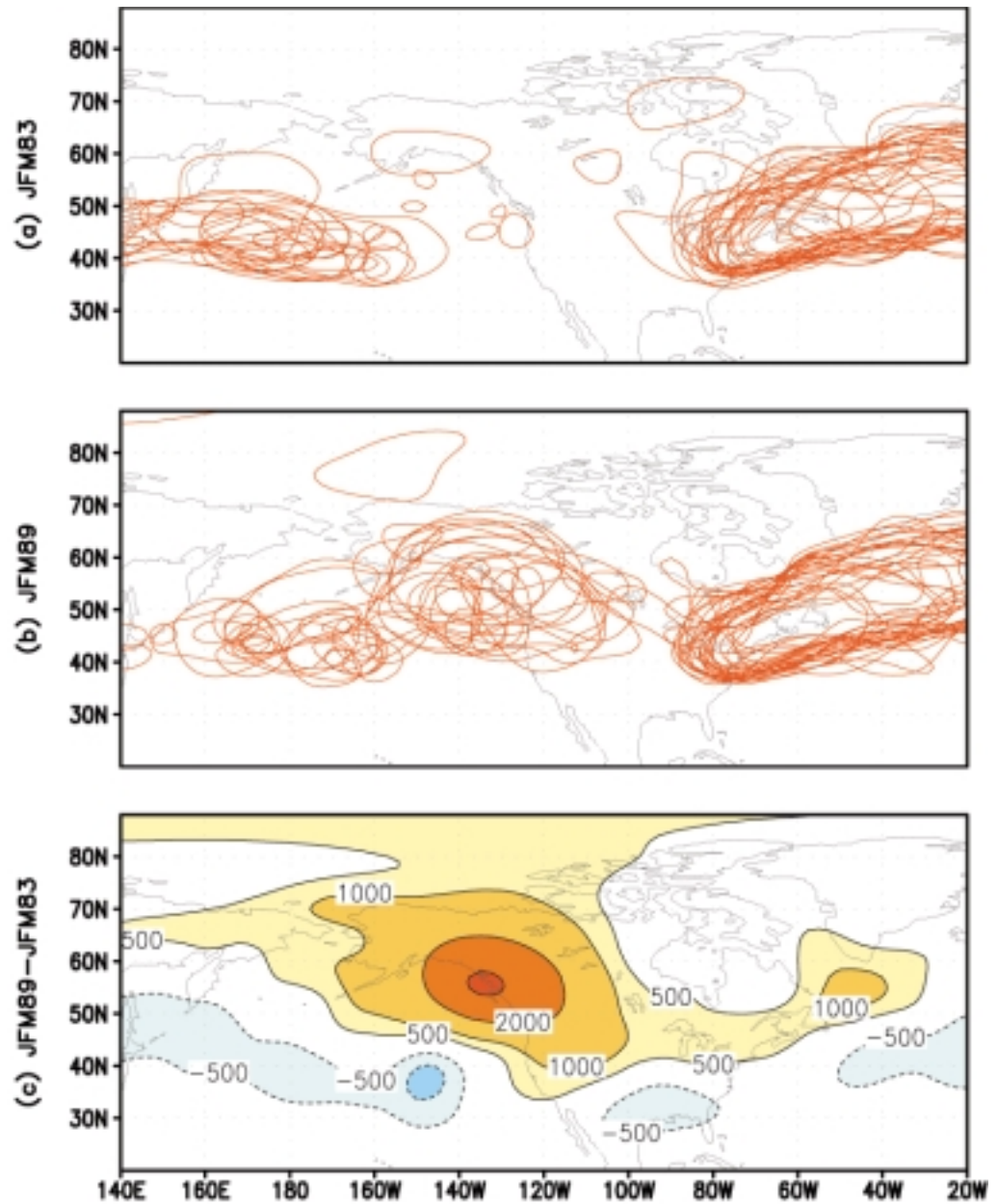


Figure 25: (a) The variance of the 1983 500 mb height field filtered to retain time scales less than 10 days. The different curves represent the 6000  $\text{m}^2$  contour of the JFM mean weather variance for the 27 cases. (b) The same as (a) but for 1989. (c) The difference (1989-1983) in the mean weather variance. Units are  $\text{m}^2$ .

Schubert, S. D., M. J. Suarez, Y. Chang, and G. Branstator, 2000: The impact of ENSO on extratropical low frequency noise in seasonal forecasts. Submitted to *J. Climate*.

## *Hurricanes*

### **High-Resolution Simulations of Hurricanes**

Hurricanes derive much of their energy from the exchanges of heat and moisture near the ocean surface. However, observations of these exchanges in the inner-core region of hurricanes are rare. This lack of data forces modelers to use boundary layer parameterizations that apply largely to lower wind-speed conditions. We need to know how our hurricane simulations are affected by our assumptions regarding the character of surface fluxes and vertical mixing within the boundary layer. We may then understand the limitations of current assumptions and have some direction for future observational studies.

We used a research-quality mesoscale model capable of representing multiple scales simultaneously (from the synoptic to the cloud scale) to simulate the intensification of Hurricane Bob (1991) along the eastern coast of the United States (Figure 26). A simulation using a horizontal grid spacing of 4 km reproduced well the track and intensity of the storm. Simulations using several different parameterizations of atmospheric boundary layer processes reveal a strong sensitivity of the simulated hurricane intensity (Figure 27) and precipitation structure to the specification of the exchanges of heat, moisture, and momentum near the sea surface. The study identifies key aspects of the boundary layer parameterizations that contribute to or inhibit intensification of the hurricane. The study suggests possible improvements to the parameterizations and areas of further research.

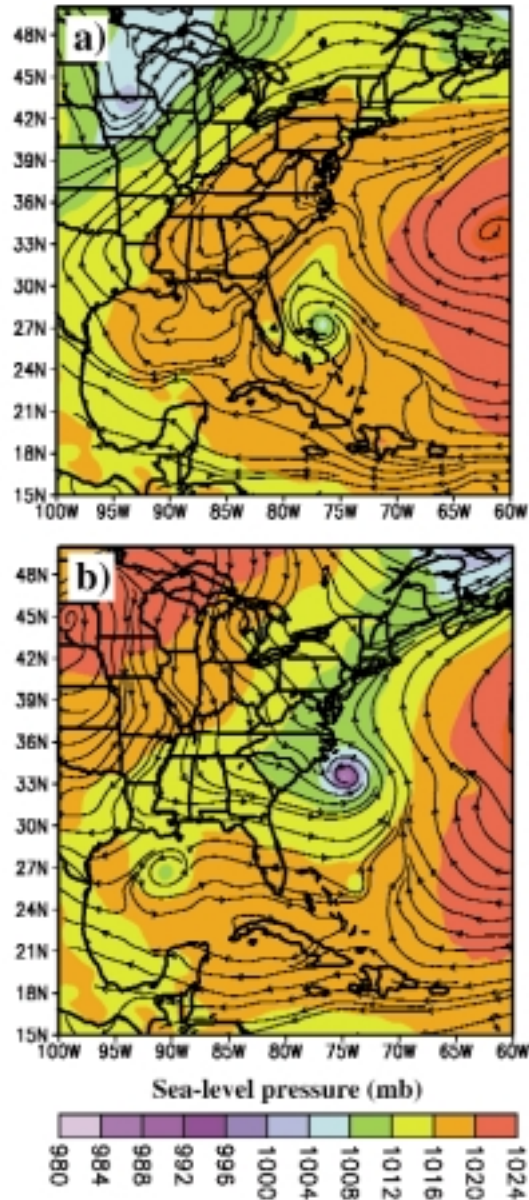
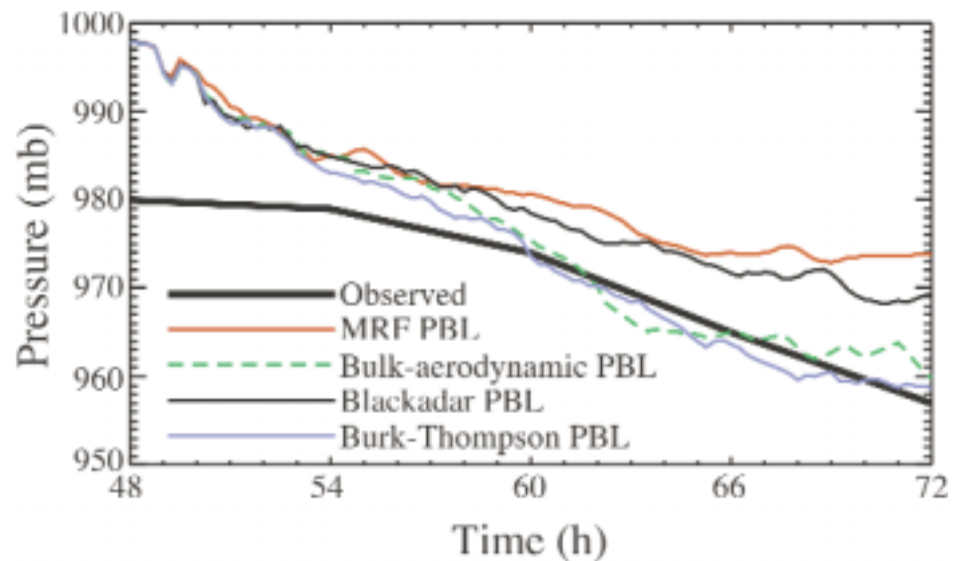


Figure 26. Simulated sea-level pressures (color shading) and 850-mb streamlines for forecasts at 24 and 72 h (initial time at 0000 UTC 16 August 1991) from a simulation using a 36-km grid spacing. Panel (a) shows the initial stages of the hurricane as it forms just north of the Bahamas. Panel (b) shows Hurricane Bob near its maximum intensity just southeast of the North Carolina coast.



**Figure 27.** Time series of Hurricane Bob's minimum central pressure, a measure of the storm's intensity, from observations (thick black line) and from simulations (thin lines). The simulated pressures are from 24 h simulations using a 4 km grid and using various boundary layer parameterizations. During the initial 6 h, the simulations show nearly identical pressure falls, but after 6 h, the solutions diverge significantly. The Medium-Range Forecast (MRF) model and Blackadar boundary layer schemes produce the weakest storms while the bulk-aerodynamic and Burk-Thompson boundary layer schemes yield the strongest storms. The differences in intensity are related mainly to differences in the parameterizations of surface moisture and momentum fluxes, but the manner in which vertical mixing in the boundary layer is parameterized also contributes to these differences.

Braun, S. A., and W.-K. Tao, 1999: Sensitivity of high-resolution simulations of Hurricane Bob (1991) to planetary boundary layer parameterizations. (Submitted to *Monthly Weather Review*).

### Numerical Simulations of Hurricanes Using a High-Resolution Global Model

Laboratory scientists have demonstrated the feasibility of simulating and forecasting hurricanes and intense tropical cyclones using a novel high-resolution General Circulation Model jointly developed by NASA/GSFC and the NCAR.

This joint NASA/NCAR global model is designed as a unified modeling system that is suitable not only for long-term, low-resolution climate change assessments but also for high-resolution weather predictions and data assimilation. What major advantage do we gain by using a global modeling system for simulation, prediction, and, ultimately, data assimilation of hurricanes? No lateral boundary conditions need to be specified. Therefore, we can better simulate and better understand the interaction between hurricane-scale and synoptic-scale motions.

Based on the highly accurate, finite-volume numerical algorithms developed at GSFC, this model is capable of simulating the complete life cycle of a hurricane from its formation to the ultimate dissipation at the relatively coarse resolution of about 55 km. As shown in Figure 28, the formation of a distinct eye-wall and the spiral rain-bands are simulated with unprecedented details for a global model.

Further development to the modeling system includes coupling to a global data assimilation system. This coupling will enable scientists to assimilate satellite data (e.g., TRMM and QuikSCAT) into the model for theoretical studies as well as for the practical application of predicting the formation, track, and intensity of hurricanes.

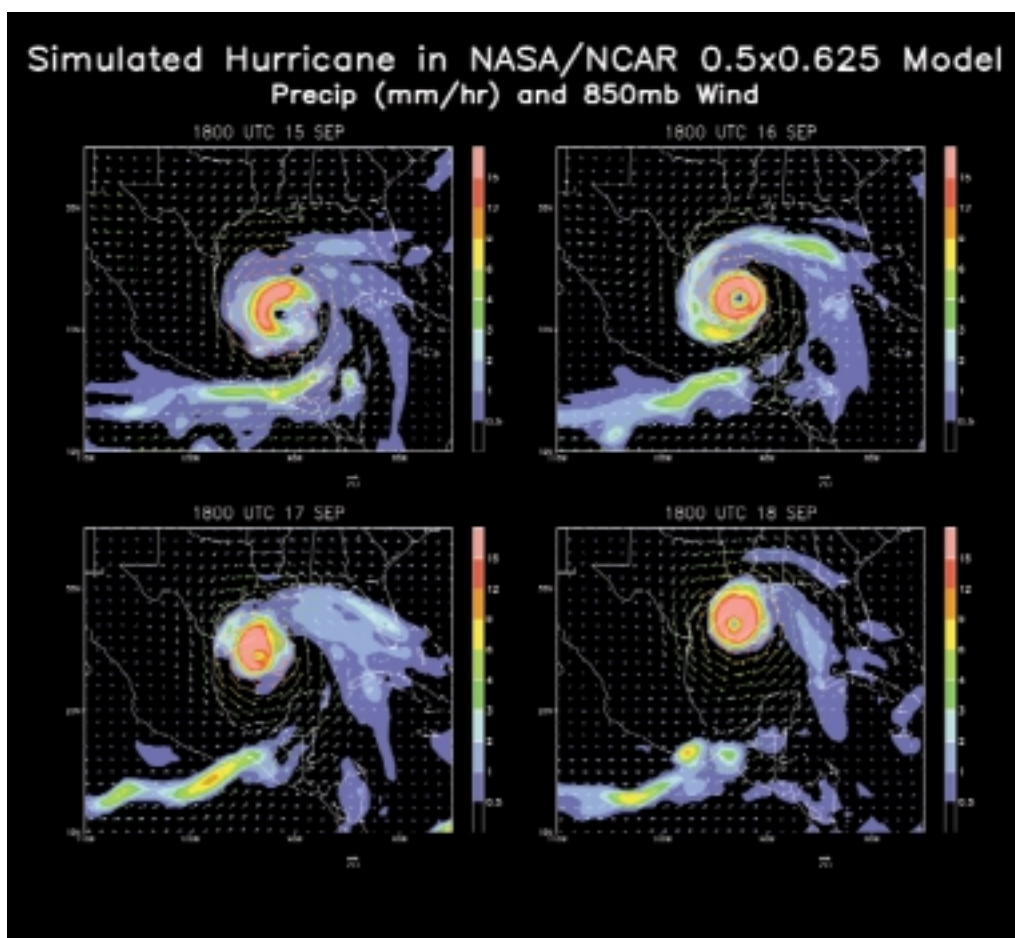


**Figure 28.** Simulated hurricane generated by the NASA/NCAR model at the 0.5x0.625 degree horizontal resolution (roughly 55 km). Instantaneous precipitation was shaded according to intensity (see color bar). This is one of many examples of intense tropical cyclones simulated in a multiyear run.

Lin, S. J., and R. B. Rood, 1998: A flux form semi-Lagrangian general circulation model with a Lagrangian control-volume vertical coordinate. Rossby-100 Symposium.

*Physical Processes***Goddard Cumulus Ensemble (GCE) Model as a Physics Resolving Process Model**

The highest science priority identified in the Global Change Research Program (GCRP) is the role of clouds in climate and hydrological systems. Accordingly, the Global Energy and Water Cycle Experiment (GEWEX) formed the GEWEX Cloud System Study (GCSS) specifically to study the effects of clouds. Cloud resolving models (CRMs) were chosen as the primary approach.

Recently, Laboratory scientists used several CRMs to study the tropical water and energy cycles and their role in the climate system. Two CRMs produced different quasi-equilibrium states (warm and humid vs. cold and dry) even though both used similar initial thermodynamic profiles, horizontal wind, and fixed SST. The GCE model showed that the differences in the CRM-simulated quasi-equilibrium state can be attributed to the treatment of atmospheric horizontal wind throughout the integration. The model that had weaker surface wind (caused by the convective mixing) produced a cooler and less humid thermodynamic equilibrium state (see Figure 29). Consequently, the cooler and less humid equilibrium state had smaller latent heat fluxes from the ocean. Current climate models do not account at all for convective momentum transport processes.

We've also used the GCE model to investigate the trigger of moist convection over heterogeneous land surface domains (inhomogeneous distribution of land usage). Simulation results and theoretical applications identified important variables (i.e., patch size of land, horizontal gradient in the heat fluxes from land, the atmospheric background wind, planetary boundary layer height, and thermodynamic properties of the boundary layer). These variables can be used to represent the convection generated by heterogeneous land surfaces in regional- and global-scale atmospheric models.



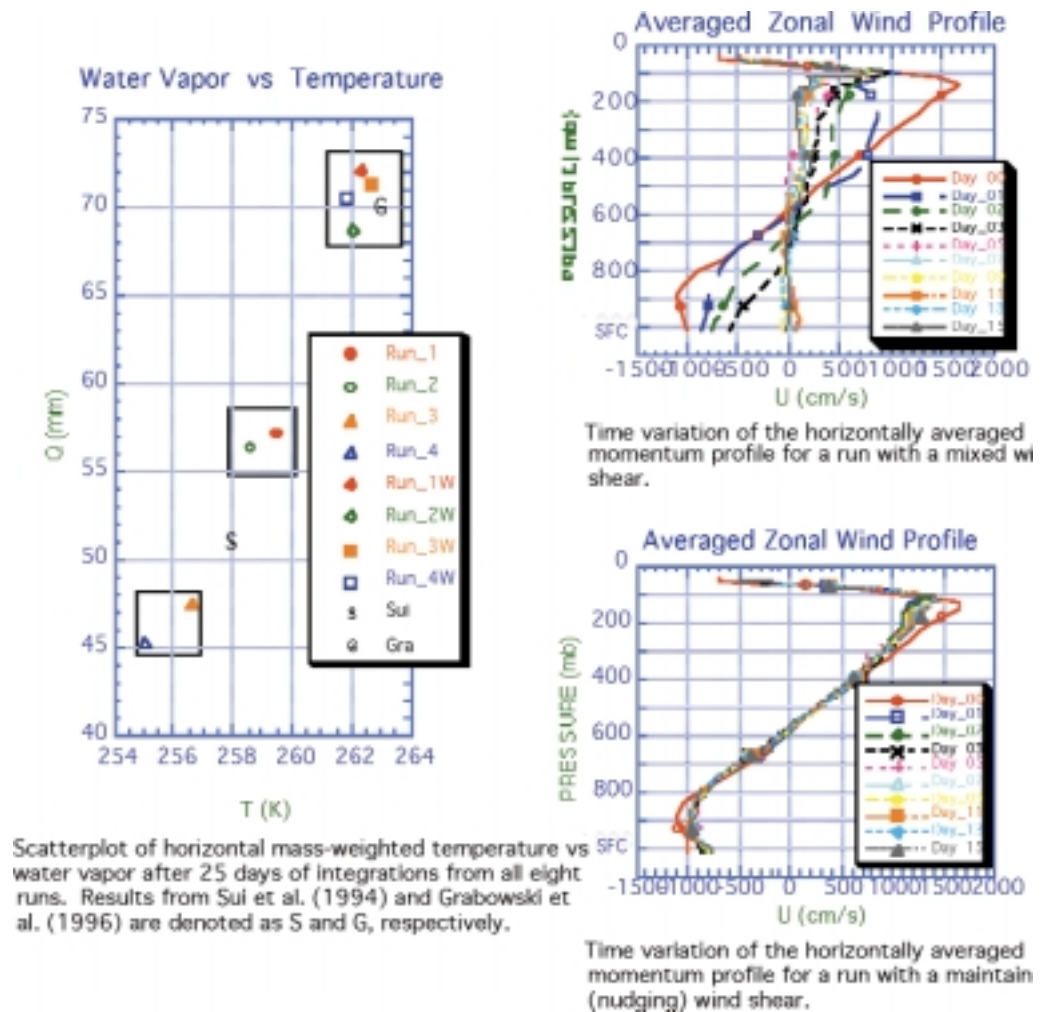


**Figure 29.** Left Panel: Scatter plot of mass-weighted temperature and water vapor. G and S, respectively, denote warm/humid and cold/dry tropical quasi-equilibrium states. Upper-right and lower-right panels show the model horizontal winds both allowing and not allowing convective momentum transport processes, respectively.

Tao, W.-K., J. Simpson, C.-H. Sui, C.-L. Shie, B. Zhou, K. M. Lau, and, M. Moncrieff, 1999: On equilibrium states simulated by Cloud-Resolving Models. *J. Atmos. Sci.*, **56**, 3128-3139.

Lynn, B. H., W.-K. Tao and F. Abramopoulos, 1999: A parameterization for the triggering of landscape generated moist convection, Part I: Analyses of high resolution model results. *J. Atmos. Sci.*, accepted.

Lynn, B. H., W.-K. Tao and F. Abramopoulos, 1999: A parameterization for the triggering of landscape generated moist convection, Part II: Zero and first order closure. *J. Atmos. Sci.*, accepted.



## Planetary Sciences

### Galileo Mission Highlights

Laboratory scientists have improved their estimate of the abundance of noble gases on Jupiter. Their new results will enhance our understanding of Jupiter's formation and, by analogy, the formation of giant planets around other stars.

The improved estimate of Jupiter's noble gases arises from ongoing analysis of data from the Galileo Probe Neutral Mass Spectrometer (GPMS) and from post-encounter calibration studies carried out on the Engineering Unit (EU) of the GPMS. Figure 30 summarizes the results. The figure shows the abundances of noble gases and other Jovian elements relative to the major species, H, ratioed to the solar value.

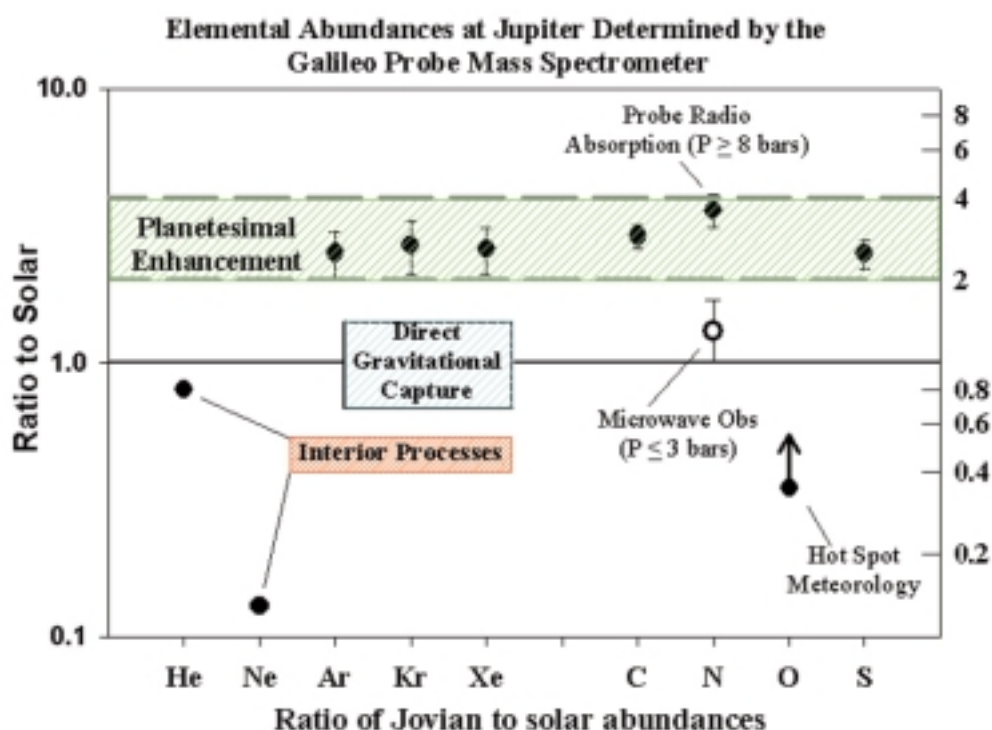


**Figure 30.** Models of solar nebular evolution suggest that the giant planets formed by accretion of the equivalent of several earth masses of planetesimals early in their development. Direct gravitational capture of gases not trapped in planetesimals could occur only when a large enough mass had converged. Planetesimals formed inward of the Uranus-Neptune region of the solar nebula, such as those that eventually were ejected to the Oort cloud, are expected to be highly depleted of argon and nitrogen since these gases are not efficiently trapped in ices formed at 50 K or higher. In fact, nitrogen depletion in at least one planetesimal was confirmed by observations of Halley's comet in 1986.

The helium and neon ratios shown above would be expected to be solar in the absence of fractionation of these elements into the interior of Jupiter. The surprisingly high values of argon and nitrogen suggest that the planetesimals that contributed to Jupiter

formed at temperatures lower than approximately 30K. Otherwise argon and nitrogen should fall much closer to the “direct gravitational capture” line shown in the figure.

Owen et al. [1999] have postulated several new scenarios for Jupiter’s formation based on these observations. These are (a) formation of Jupiter at great distances from the sun ( $>30$  AU) and subsequent inward migration (several recently discovered giant planets are very close to their sun), (b) a colder solar nebula than was previously assumed, and (c) early formation of planetesimals in the interstellar cloud that survived intact in the solar nebula. These possibilities can be explored by further theoretical models and by future missions to comets and the atmospheres of other giant planets.

Mahaffy, P. R., H. B. Niemann, A. Alpert, S. K. Atreya, J. Demick, T. M. Donahue, D. N. Harpold, and T. C. Owen, 1999: Noble gas abundance and isotope ratios in the atmosphere of Jupiter from the Galileo Probe Mass Spectrometer. Submitted to *JGR*.